Using ChemCam LIBS data to constrain grain size in rocks on Mars: Proof of concept and application to rocks at Yellowknife Bay and Pahrump Hills, Gale crater

Frances Rivera-Hernández, Dawn y Sumner, Nicolas Mangold, Kathryn M Stack, Olivier Forni, Horton Newsom, Amy Williams, Marion Nachon, Jonas L'Haridon, Olivier Gasnault, et al.

Using ChemCam LIBS data to constrain grain size in rocks on Mars: Proof of concept and application to rocks at Yellowknife Bay and Pahrump Hills, Gale crater

Frances Rivera-Hernández[1], Dawn Y. Sumner[1], Nicolas Mangold[2], Kathryn M. Stack[3], Olivier Forni[4], Horton Newsom[5], Amy Williams[6], Marion Nachon[1], Jonas L'Haridon[2], Olivier Gasnault[4], Roger Wiens[7], Sylvestre Maurice[4]

[1] Earth and Planetary Sciences Department, University of California, Davis, CA, USA, *friverah@ucdavis.edu*
[2] Laboratoire de Planétologie et Géophysique de Nantes, Université de Nantes, Nantes, France
[3] Jet Propulsion Laboratory, California Institute of Technology, Pasadena, CA, USA
[4] IRAP, Université de Toulouse, CNRS, UPS, CNES, Toulouse, France
[5] University of New Mexico, Albuquerque, NM, USA
[6] Department of Physics, Astronomy & Geosciences, Towson University, Towson, MD, USA
[7] Los Alamos National Laboratory, Los Alamos, NM, USA

Corresponding author: Dr. Frances Rivera-Hernández
Email: Frances.Rivera-Hernandez@Dartmouth.edu
Telephone: 787-557-1788
Mailing Address:
Dartmouth College
Dept. of Earth Sciences
Hinman Box 6105
Hanover, NH 03755

Abstract. Grain size in martian sedimentary rocks can be constrained using point-to-point chemical variabilities in Laser Induced Breakdown Spectroscopy (LIBS) data from the ChemCam instrument on the Mars Science Laboratory (MSL) *Curiosity* rover. The diameter of each point vaporized by the ChemCam laser is in the range of medium to coarse sand in size. Thus, rocks with grains smaller than the laser spot size produce bulk rock compositions at each LIBS point and low point-to-point chemical variability among LIBS points. In contrast, analyses of rocks with grains about the size of the spot or larger contain contributions from individual grains at each point and often have high point-to-point chemical variability. The Gini index, a statistical parameter, was used to calculate the point-to-point chemical variability in major-element oxide compositions derived from the ChemCam LIBS data. The variability of each oxide was then combined to derive a Gini mean score, G_{MEAN}, for each LIBS observation. A standard procedure was developed and validated using observations of sedimentary rocks of various grain sizes from the Yellowknife Bay formation and the Pahrump Hills member of the Murray formation in Gale crater. Overall, finer-grained rocks have smaller G_{MEAN} than coarser-grained rocks. To calibrate grain size ranges for specific G_{MEAN} values, the LIBS major-element oxide compositions were first normalized as a group. Next, grain size estimates based on visual assessment of high-resolution images were compared to G_{MEAN} values for the same targets to create a calibrated scale. This calibrated scale was used to infer the grain size of rocks with unknown grain size. Overall, the grain sizes predicted for rocks with unknown grain size overlapped with those of known grain size from the same units and/or bedrock targets. The grain sizes inferred using the G_{MEAN} based on ChemCam LIBS data are complimentary to those determined from images and both techniques can be used to improve interpretations of the depositional environments of rocks analyzed by *Curiosity* and future Mars missions with LIBS, such as the Mars 2020 rover.

Keywords: Mars, grain size, sedimentary rocks, LIBS, Mars Science Laboratory

1. Introduction

The primary goal of the Mars Science Laboratory (MSL) mission is to characterize habitable environments of early Mars in the sedimentary record of Gale crater (e.g., Grotzinger et al., 2012). Evaluating past habitability requires reconstructing the conditions of sediment transport and deposition from sedimentary rocks with an emphasis on interpreting changes in the ancient environments. Characterizing the size of grains and their distribution in sedimentary rocks provides information about how the grains were transported, which is crucial for interpreting depositional environments. For example, laminated mudstones accumulate in environments with very low flow speeds such as lakes, whereas cross-bedded sandstones and conglomerates require higher flow speeds and are characteristic of river and beach deposits. Identifying lacustrine deposits is important as lakes both indicate a sustained presence of liquid water and commonly preserve biosignatures on Earth (Farmer and DesMarais, 1999; Summons et al., 2011). However, determining the size of sediment grains in rocks is challenging on Mars due to the resolution limits of rover image data. Whether or not grains larger than mud in size (> 62.5 μm) can be resolved in an image depends on a variety of factors, such as camera specifications, the distance of the camera from the rock, illumination, grain color contrast, and dust cover. Except for coarse-grained rocks and several well studied sites of importance (e.g., Williams et al., 2013; Edgar et al., 2017; Stack et al., 2016; Banham et al., 2018), the grain sizes of most rocks observed in *Curiosity* rover images are unknown.

To supplement the grain sizes determined using image-based analyses, Mangold et al. (2017) proposed that point-to-point chemical variabilities in ChemCam Laser Induced Breakdown Spectroscopy (LIBS) data could be used as a proxy to infer the size of grains or crystals in sedimentary and igneous rocks. This grain size proxy was validated for a few rocks sampled by the ChemCam LIBS instrument (Mangold et al., 2017), and it can be applied extensively to diverse suites of rocks once a standard procedure for its application is developed and tested.

In this paper, we evaluate the robustness and reproducibility of using ChemCam LIBS data to infer the size of grains in sedimentary rocks along the *Curiosity* traverse in two areas, informally called Yellowknife Bay (YKB) and the Pahrump Hills (PH; Fig. 1). Both regions have mudstones and sandstones (Grotzinger et al., 2014; 2015), providing an opportunity to compare and contrast the point-to-point chemical variability of rocks with similar grain size distributions. Results from this comparison were then used to develop a scale to infer the grain size distribution of rocks with known and unknown grain size. The standard procedure presented here can be applied to additional ChemCam LIBS data and to results from future Mars missions with LIBS, such as the Mars 2020 rover (Wiens et al., 2017).

2. Methods

2.1. ChemCam LIBS data

The ChemCam instrument suite consists of a LIBS and the Remote Micro-Imager (RMI) that collects co-located context images (Maurice et al., 2012a; Wiens et al., 2012). The LIBS uses a pulsed laser to ablate small spots (~0.4-0.6 mm in diameter), commonly in lines of 5 to 10 points or matrixes of 3x3 points, on targets 2 to 7 m from the rover (Maurice et al., 2012a; Wiens et al., 2012). The measurement points are typically spaced by 2 mrad, which represents a sampling every 6 mm for a target at 3 m. The laser spot size increases with distance from the rover, affecting the amount of material that is ablated by the laser and thus analyzed by ChemCam (Maurice et al., 2012b). The light from the ablated plasma at each spot is passed

through three spectrometers to acquire an atomic emission spectrum in the wavelength ranges: 240-342 nm, 382-469 nm, and 474-906 nm (Maurice et al., 2012a; Wiens et al., 2012). When the plasma cools, atoms in the plasma can recombine and molecular emission lines can also be observed (e.g., Cremers and Radziemski, 2013; Anderson et al., 2017). For each laser pulse, a LIBS spectrum is acquired. Commonly, there are 30 laser shots per point, with the first laser shots removing surface dust and coatings (Wiens et al., 2013). For each point, the weight percent (wt.%) of eight major-element oxides (SiO_2, TiO_2, Al_2O_3, FeO_T, MgO, CaO, Na_2O, and K_2O) are derived from multivariate analysis comparing the elemental emission lines of martian targets to Earth standards (Clegg et al., 2009; 2017; Cousin et al., 2011; Wiens et al., 2013). FeO_T refers to total iron, including both FeO and Fe_2O_3, as these are not distinguishable using ChemCam. The first five shots per LIBS point are removed to exclude the influence of dust (Lasue et al., 2016) and the other 25 shots are used to calculate the mean, root mean square error (RMSE), and standard deviation of every major-element oxide (Wiens et al., 2013; Clegg et al., 2017). If the modeled spectrum can be reproduced with all eight major-element oxides, then the total sum of their weight percent equals 100% with error in accuracy of less than 10% (Clegg et al., 2017). When the major-element oxide total is less than 100%, there is a missing component in the model, for example from an abundance of Cl, H, F, Li, Sr, Ba, Rb, Mn, P, S, Ni, Zn, or Cr. Thus, the sum of the major-element oxides is not normalized to 100%. An abundance of sulfate minerals from diagenesis (Nachon et al., 2014; 2017) is the most common cause for oxide totals of less than 100%. Only the major-element oxides are discussed here.

To verify the quality of the LIBS data, calibration targets onboard *Curiosity* are regularly analyzed (Fabre et al., 2011; Vaniman et al., 2012). Precision for the ChemCam LIBS data can be determined by quantifying the variability between repeated measurements either on the calibration targets, or on relatively homogeneous and fine-grained rock exposures on Mars (i.e., mudstones; Mangold et al., 2015; Clegg et al., 2017). The accuracy of analyses is predicted using a RMSE for a representative test set of rock calibration targets, chosen such that each major-element oxide has distributions similar to the full set of rock standards used to generate the regression models in the multivariate analysis (Clegg et al., 2017). Typically for the ChemCam LIBS, accuracy is higher in magnitude than precision. For example, for the first 801 sols of the MSL mission, the total RMSEs (accuracy) for the Shergottite calibration target are (in wt.%): SiO_2=5.04, TiO_2=0.14, Al_2O_3=4.02, FeO_T=5.28, MgO=1.39, CaO=2.56, Na_2O=1.09, and K_2O=0.67 (Clegg et al., 2017). Whereas, precision values calculated from sols 271, 352, and 357, for the same major elements as above are 1.53, 0.14, 0.57, 1.83, 0.49, 0.42, 0.49, and 0.14 wt.% respectively (Blaney et al., 2014). As this study depends on point-to-point LIBS variabilities, precision error is propagated in our calculations (see Section 2.2 and the Appendix).

2.2. ChemCam LIBS data as proxy for grain size

The size of grains in a rock can be constrained using LIBS data because the diameter of each point vaporized by the ChemCam laser is known (medium to coarse sand in size, with increasing distance to the target). If a rock has grains considerably smaller than the laser spot diameter, the bulk composition of the rock is analyzed at each point (Anderson et al., 2011; McCanta et al., 2013; 2017) and little to no point-to-point chemical variability is observed (Fig. 2; Sivakumar et al., 2014). However, if a rock has grains similar in size or larger than the laser spot diameter, each point can potentially have a different composition reflecting individual grain compositions (McCanta et al., 2013; 2017). A large number of spots would have to be analyzed to get a bulk composition for the rock (Fig. 2; Anderson et al., 2011). If a rock has grains much

larger than the distance between the LIBS points (typically ~6 mm; pebble or larger), the laser may hit the same grain more than once, reducing variability, though these grains should be resolved in images. If a rock has grains of uniform composition, regardless of grain size, the LIBS data will exhibit little to no point-to-point chemical variability and grain size cannot be constrained by this method.

For coarse-grained rocks with non-uniform compositions and grains smaller than fine gravel in size, the presence of grains may be inferred by looking at heterogeneities in the LIBS data (Sivakumar et al., 2014; Mangold et al., 2017). Mangold et al. (2017) proposed that these heterogeneities can be quantified and used as a proxy for inferring grain size by implementing a statistical measurement called the Gini index (*G*). The Gini index is commonly used to characterize variations across a population, such as inequalities in wealth (Gini, 1921). The Gini index varies from 0 to 1, where G=0 expresses complete equality or uniformity and G=1 complete inequality. Applied to grain size, a G=0 suggests the rock has grains much smaller than the laser spot size (mud) or are of a uniform composition, and if G=1, then the laser hit distinct compositions at each point and the grain size is likely larger than the spot size. To use the Gini index as a proxy for grain size, we developed the Gini index mean score (GIMS), with a slightly different implementation from Mangold et al. (2017). The values reported here are averages, G_{MEAN}, calculated by applying an arithmetic mean to the Gini indices of each major-element oxide, G_i, except TiO_2. For all of the rock targets, the weight percent of each oxide was normalized based on the range of values in all samples before calculating G_i and G_{MEAN} (details in *Appendix*). Thus, G_i and G_{MEAN} depend on the details of the normalization, and different rocks can only be compared to each other if they are similarly normalized. When different normalizations are used, Gini index values may be different for the same grain size and thus, Gini index values reported in Mangold et al. (2017) or in other publications may not correspond to the same grain sizes presented here using the GIMS. Two different standard deviation metrics were calculated for each G_{MEAN}, STDr and STDc, both derived from standard deviations of every major-element oxide per LIBS point. For STDr, the standard deviations are based on variations in the shot-to-shot LIBS measurements on the rock targets used in the GIMS analysis (Supplemental Table 1), whereas for STDc, the values are scaled standard deviations derived from the Shergottite calibration target on *Curiosity* (see Blaney et al., 2014). The standard deviations for each LIBS point and major-element oxide, were propagated to errors on G_{MEAN} using an iterated bootstrap with 1000 iterations. STDr and STDc are 0.00-0.02 and 0.00-0.01, respectively, which is much lower than the variations due to rock composition (G_{MEAN}=0.02-0.29; Table 2). STDr is used in the text and figures due to its slightly larger variation. Interestingly, the lowest G_{MEAN} value gives another precision estimate because mudstones are predicted to have a G_{MEAN}=0 (completely homogenous). The lowest calculated G_{MEAN} was 0.02 on YKB mudstones, consistent with the 1σ STDr of 0.00-0.01 on those samples (Table 2), suggesting that instrumental precision error is smaller than typical variations in LIBS spot compositions.

G_{MEAN} scores need to be calibrated to grain size using samples with both LIBS data and appropriate corresponding images, with the approximate compositions and mineral assemblages present in the unknown rocks. By calculating the G_{MEAN} of rocks with known grain size, G_{MEAN} ranges can be scaled to grain sizes ranges (Section 5.2). Other rocks with unknown grain size can then be compared to this scale to constrain their grain size. By comparing rocks with known grain size that were not involved in the scaling, the robustness of the GIMS can be evaluated for a specific suite of rocks.

In addition to grain size, other factors can also cause point-to-point heterogeneities and homogeneities. Regardless of grain size, if a rock has grains with a uniform composition, then the rock will have little to no point-to-point chemical variability, and thus a low G_{MEAN}. This is not expected for sedimentary rocks along *Curiosity's* traverse, as these contain a diverse suite of basaltic grain compositions, including pyroxene, feldspar, olivine, other mafic minerals, and glass (Vaniman et al., 2013; Sautter et al., 2014; Mangold et al., 2016; Cousin et al., 2017; Rampe et al., 2017). Heterogeneities in composition in a rock can be caused by contamination by loose sediment (sand and dust), diagenetic features, and intergranular cements. Different steps were taken to minimize the contribution of these heterogeneities in our analyses. First, RMI images were used to identify where the laser hit a rock at each LIBS point. Those points that sampled visually resolvable diagenetic features, loose sediment, cracks, and sharp edges were excluded from the GIMS analyses. Targets with abundant diagenetic features in the scene, regardless of whether or not the laser hit the features, were also excluded. Next, points with < 87% major-element oxide totals were removed (see Appendix), as low oxide totals commonly suggest the presence of a non-resolvable diagenetic contribution (e.g., Jackson, 2016), such as a cement (Newsom et al., 2017; Nellessen et al., 2018) or diagenetic feature (e.g., sulfate veins; see Section 2.1). Only rock targets with more than five points were used for the GIMS analysis, as that is the minimum number of points necessary to obtain a statistically significant Gini index result (Mangold et al., 2017). Thus, the GIMS was only applied to select rocks that passed the filtering process. Prescreening the rock targets allows a reproducible, standard procedure to be applied to all targets.

The filtered ChemCam LIBS data from 50 rocks at YKB and 15 at PH were used in the GIMS analysis (Supplemental Table 1). The ChemCam targets are informally named by the MSL science team and those names are used here to reference the rock targets. The Planetary Data System also includes this classification scheme. Following the format of target names in the Planetary Data System, target names containing multiple words include underscores (i.e., rock_name). When more than one LIBS analysis is acquired on the same rock target, underscores are used to enumerate each analysis location on the rock (i.e., rock_name_1, rock_name_2).

2.3. Image Data Sets

Previous work done to constrain grain sizes at YKB and PH (see Section 3.1; Blaney et al., 2014; Grotzinger et al., 2014; 2015; Mangold et al., 2015; Anderson et al., 2015; Stack et al., 2016; Edgar et al., 2017), coupled with additional textural analysis performed in this study, enables calibration of the GIMS for these units. Limitations on grain size observed in rover images depend on the camera characteristics, the target distance, illumination, and amount of dust cover. Images taken by MAHLI and RMI were used to measure grain size, whereas images taken by Mastcam were used as context for the RMI and MAHLI images and to document sedimentary textures, such as cross-bedding.

The RMI has an angular pixel size of 0.0195 mrad/pixel, a circular field of view of 20 mrad over 1024 × 1024 pixels and produces black and white images that are co-located with the LIBS analyses (Le Mouélic et al., 2015). Depending on the distance of the rover to the LIBS target, the spatial resolution of an RMI image can range from ~0.04 to ~0.15 mm/pixel (Le Mouélic et al., 2015). Most ChemCam LIBS measurements are made at ~2-3 m distance, restricting the finest grain size that can be resolved to fine to medium sand. In addition, the RMI's narrow depth of focus (~1 cm at 2 m distance; Le Mouélic et al., 2015) makes it difficult to resolve grains outside the best focus area in a RMI image mosaic (Anderson et al., 2014).

However, RMI images are the best for characterizing grain sizes for our analyses as they show the regions targeted by the ChemCam LIBS and the RMI resolution is compatible with the laser spot size.

The Mastcams are a two-instrument suite that provide color images (Malin et al., 2016; Bell et al., 2017). The left Mastcam (M-34) has a 34 mm focal length, 0.22 mrad/pixel, and 18.4° × 15° effective field of view over 1600 × 1200 pixels (Malin et al., 2016; Bell et al., 2017). The right Mastcam (M-100) has a 100 mm focal length, 0.074 mrad/pixel, and an effective field of view of 6.3° × 5.1° over 1600 × 1200 pixels (Malin et al., 2016; Bell et al., 2017). Most targets investigated by ChemCam have corresponding Mastcam images, typically taken by the M-100, and these can sometimes be merged with the RMI images to provide color information for the scene. The M-100 can resolve coarse sand sized features (~500 μm; larger than the laser spot size) at a distance of 3 m.

The MAHLI is mounted on the rover's arm, and it is capable of color and stereo imaging by physical offset of the arm between images (Edgett et al., 2012). It has a macrolens that can focus over a range of distances from 2.1 cm to infinity (Edgett et al., 2012). At the minimum working distance (2.1 cm), MAHLI has a 18.4 mm focal length, 26.8° × 20.1° effective field of view over 1600 × 1200 pixels, and spatial resolution of ~14 μm/pixel (very coarse silt in size; Edgett et al., 2012). MAHLI images are commonly used for grain size and other textural analyses, as well as to provide context imaging for other contact science. It takes ~2.5 pixels to enable a confident grain detection. In this study only rock surfaces brushed by the Dust Removal Tool are used for grain size analyses at the coarse silt to very fine sand scale because dust can mask the underlying surface and differentiating between loose dust grains and grains embedded in a rock becomes difficult. Due to the significant time and power resources needed to deploy the rover's arm, MAHLI is primarily used for high-priority science at strategically planned stops along the rover traverse (Vasavada et al., 2014; Edgett et al., 2015; Yingst et al., 2016). Thus, image data from the other cameras are necessary to provide a more continuous record of the sedimentary textures and structures of the rocks encountered along the traverse. However, the other cameras can only resolve grain sizes typically coarser than fine sand, which is insufficient for the desired environmental interpretations.

3. Geologic setting

The *Curiosity* rover landed in Gale crater on 6 August 2012 at a site called Bradbury Landing (Fig. 1). Gale crater is located in the equatorial region of Mars (137.7°E, 5.44 S) along the crustal dichotomy between the smooth northern lowlands and the cratered southern highlands. The crater is ~154 km in diameter, and its center it has a ~5 km high layered mound, informally called Mount Sharp (formally named Aeolis Mons), that has hematite-, phyllosilicate-, and sulfate-bearing stratigraphic layers (Malin and Edgett, 2000; Milliken et al., 2010; Fraeman et al. 2013; 2016). Based on crater counts, Gale crater formed near the Noachian-Hesperian transition (3.6 Ga; Le Deit et al., 2013, Thomson et al., 2011), and the crater-filling material may have accumulated through to the early Hesperian (Thomson et al., 2011; Grant et al., 2014; Palucis et al., 2014; Grotzinger et al., 2015). *Curiosity* landed at the distal end of the Peace Vallis alluvial fan, which is sourced from the northern crater rim (Palucis et al., 2014). After landing, the *Curiosity* rover performed analyses at various waypoints on its journey up Mount Sharp, including the outcrops of the YKB and PH member of the Murray formation (Fig. 1b). The YKB and PH regions include important facies characterized by the rover, and a number of rocks were

co-investigated by ChemCam, Mastcam, and MAHLI at these locations. Such targets provide good controls for connecting G_{MEAN} and grain sizes determined from images.

3.1. Sedimentology and stratigraphy

Yellowknife Bay formation: On sol 125, 445 m east and 14 m below Bradbury Landing, *Curiosity* encountered the first outcrops of the ~5.2 m thick YKB formation (Fig. 3). The rover investigated the region in detail until sol 324. In ascending order in elevation, the three members of the YKB formation are informally named the Sheepbed, Gillespie Lake, and Glenelg members (Grotzinger et al., 2014; 2015). The mean dip of the rocks at YKB and PH regions is approximately horizontal, which allows elevation to be used as a proxy for stratigraphic height (Grotzinger et al., 2015). The Sheepbed member consists of mudstones interpreted to be lacustrine in origin (Grotzinger et al., 2014; 2015). The Gillespie Lake member consists primarily of well-cemented medium to coarse sandstones with occasional pebbly sandstones. It generally has a massive appearance, though poorly defined cross-bedding was observed (Grotzinger et al., 2014; Mangold et al., 2015). The sediments of the Gillespie Lake sandstones are interpreted as deposited in a distal fluvial environment (Grotzinger et al., 2014). The Glenelg member is exposed at four main outcrops: Point Lake, Shaler, Rocknest, and Bathurst Inlet. Rocks from Bathurst Inlet were not considered in our analyses. The rocks of the Point Lake outcrop exhibit pitted textures with voids ranging from millimeters to several centimeters in diameter (Grotzinger et al., 2014; 2015). They are interpreted to be coarse to very coarse sandstones based on the identification of a few grains that were 0.5-2.0 mm in size (Mangold et al., 2015). The Shaler outcrop consists of well-exposed cross-stratified coarse sandstones with granules interpreted to be fluvial in origin (Grotzinger et al., 2014; 2015; Anderson et al., 2015; Edgar et al., 2017). The rocks of the Rocknest outcrop have either massive or finely laminated textures, including low angle cross-lamination, and some exhibit circular to ovoid pits several millimeters in diameter (Blaney et al., 2014; Grotzinger et al., 2014; Mangold et al., 2015). They are interpreted as either siltstones or sandstones.

Pahrump Hills member, Murray formation: On sol 750, *Curiosity* encountered the first exposures of lower Mount Sharp stratigraphy at an area informally called Pahrump Hills, the lowest member of the Murray formation examined by the rover (Grotzinger et al., 2015). The rover investigated the region in detail until sol 940, performing three successive traverses of the outcrop. The PH section is ~13 m thick and had 9 areas studied in detail, in ascending order in elevation: Shoemaker, Confidence Hills, Pink Cliffs, Book Cliffs, Alexander Hills, Chinle, Telegraph Peak, Whale Rock, and Salsberry Peak (Fig. 4; Stack et al., 2016). Rocks from: Shoemaker, Pink Cliffs, Telegraph Peak, and Salsberry Peak were not included in our analyses. The lower PH section, from Shoemaker to Telegraph Peak, consists of laminated mudstones and/or siltstones with grains smaller than the limit of resolution of MAHLI images (coarse silt/very fine sand; Grotzinger et al., 2015; Stack et al., 2016). The section includes the cross-laminated sandstone facies of Whale Rock (Grotzinger et al., 2015; Stack et al., 2016). The association of facies at PH is consistent with a coarsening upward trend and is interpreted to be a fluvio-lacustrine depositional environment, with the mudstones representing lacustrine deposition and sandstones fluvial or subaqueous deposition on the foreslope of a delta (Grotzinger et al., 2015).

3.2. Overview of the chemistry and diagenetic history of Yellowknife Bay and Pahrump Hills

While the rocks of both YKB and PH have bulk basaltic compositions (Grotzinger et al., 2015), they are chemically distinct from each other with varying diagenetic histories (McLennan et al., 2014; Ming et al., 2014; Stack et al., 2014; Vaniman et al., 2013; Mangold et al., 2015; Nachon et al., 2017). Compared to PH, the rocks of YKB generally have mean compositions more similar to average martian crust (McLennan, 2012), with lower SiO_2, and higher MgO, FeO, and CaO (see Supplemental Table 1; McLennan et al., 2014; Mangold et al., 2015; Mangold et al., 2016; Nachon et al., 2017). There are compositional variations within both formations as well (see Supplemental Table 1; Mangold et al*.,* 2015; Rampe et al., 2017). For example, the Whale Rock outcrop in PH has relatively high CaO, up to 15.2 wt %, compared to the mean of YKB and PH, 5.3 and 4.97 wt%, respectively (see Supplemental Table 1). Variations in composition between members and formations are likely due to variations in provenance, mechanical sorting, post-depositional interaction with different diagenetic fluids, and intergranular cements (e.g., Mangold et al., 2017; Siebach et al., 2017). The GIMS calibration includes the normalization of all the LIBS data to account for regional variations of major-element oxide weight fractions (see Appendix).

Both YKB and PH contain diverse diagenetic features (Vaniman et al., 2013; Grotzinger et al., 2014; 2015; McLennan et al*.,* 2014; Stack et al., 2014; Nachon et al., 2014; 2017; Mangold et al., 2015). At YKB, diagenetic features included solid nodules, hollow nodules, raised ridges, sulfate-filled fractures and nodules, vugs, and sedimentary dykes (Grotzinger et al*.,* 2014; Stack et al., 2014; Siebach et al., 2014; Nachon et al., 2014). Nodules were sub-mm to mm concretions and densely clustered in some locations of the Sheepbed member; however, the compositions of concretion-rich rocks were not distinct from the overall composition of other Sheepbed rocks (Stack et al., 2014). The Sheepbed member is also cross-cut by pervasive light toned Ca-sulfate veins, <2cm in width, that were less frequent in other YKB members (Nachon et al., 2014). Raised ridges at YKB were curvilinear, narrow (<1-6 mm in width and several centimeters in length) and differentially weathered relative to the surrounding rock, creating the raised relief (Siebach et al., 2014; Leveille et al., 2014). These ridges are primarily located in the Sheepbed member and have elevated Mg and Li, with some increases in Fe, Si, Cl, and Br also observed, based on ChemCam and APXS analyses (Grotzinger et al., 2014; Leveille et al., 2014).

At PH, diagenetic features included dendritic aggregates, enhanced relief features with various geometries, dark raised-ridges, and light-toned sulfate veins (Nachon et al., 2017). Enhanced relief features were enriched in MgO, and depleted in SiO and FeO compared to the host rock (Kah et al., 2015; Nachon et al., 2017). Dark raised ridges were enhanced with MgO and CaO and did not have any obvious systematic depletions in SiO or FeO (Nachon et al., 2017). Light-toned Ca-sulfate veins were a few millimeters wide and a centimeter to tens of centimeters in length. They either cross-cut the host rock or occurred aligned within coarse-grained sedimentary layers (Kronyak et al., 2015; Nachon et al., 2017). The lower outcrops of PH have evidence for diagenetic mineral precipitation, including lenticular crystal pseudomorphs (Kah et al., 2015), preferentially cemented laminae, and late-diagenetic crystal clusters. Silt to medium sand-sized dark features were pervasive in rocks from Pink Cliffs, Shoemaker, Book Cliffs, and Telegraph Peak, but it is unclear whether they are clastic grains or micro-diagenetic concretions (Stack et al., 2016). Rocks from YKB and PH with observable or suspected diagenetic features were excluded from the GIMS analysis because diagenesis can obscure the relationship between chemical variability and grain size.

4. Constraining grain size from images

Rocks with grain sizes ranging from mud to coarse sand at YKB and PH serve as standards for the GIMS calibration (Table 1). Of the calibration rocks, 13 are in the Sheepbed member, 2 in the Gillespie Lake member, 1 in the Shaler outcrop of the Glenelg member, 3 in Confidence Hills, 2 in Book Cliffs, 3 in Chinle, and 3 in Whale Rock (Table 1). In addition to the rocks used as calibration standards from YKB, grain sizes are also reported for 11 other rocks, including some with rare resolvable grains in RMI images (Table 2).

Three main criteria were used to identify grains in images: they had to 1) be embedded in the rock, 2) have positive relief, and 3) be discrete and approximately spherical (to differentiate them from scratches). The diameters of grains were measured as their longest axes using the image-processing program ImageJ (http://imagej.nih.gov/ij/). Grain sizes were classified using the Wentworth scale (Wentworth, 1992), where very fine sand=62.5-125 μm, fine sand=125-250 μm, medium sand=0.25-0.5 mm, coarse sand=0.5-1 mm, very coarse sand=1-2 mm, very fine gravel (granule)=2-4 mm, and fine gravel (pebble)=4-8 mm. Clay and silt were grouped together as mud (62.5 μm and smaller), where coarse silt=20-62.5 μm. The finest grain size observable in RMI images is fine sand due to resolution limits. Mud was inferred for those targets that did not have resolvable grains in MAHLI images nor evidence of cross stratification in any images. Due to limited resolution of the images and to dust mantling the rocks, the median grain size of a rock might be smaller than the finest resolvable grain in an image.

5. Results

5.1. Grain size of calibration rocks using image data

All ChemCam analyses on the Sheepbed member of YKB reported here are used as standards (Table 1). The other members in YKB are characterized by having a wide range of grain sizes, and specific rock targets were picked to represent each grain size range. For rocks with fine to medium sand, the target Nanok from the Gillespie Lake member is used as a standard (Fig. 5a). Nanok has a rough texture and consists of moderately to moderately well sorted fine to medium sand with sparse coarse sand, though the coarse sand was not near the laser pits (Fig. 5a). Only <5-10 % distinct grains are resolvable in the rock with most grains too small or showing too little color contrast to resolve. Dust mantled the area near the laser pits, and it was difficult to ascertain the proportions of fine to medium sand in the RMI image. For rocks with medium to very coarse sand, the targets Gillespie_Lake_1 and Wakham_Bay are used as standards. Gillespie_Lake_1 is very poorly sorted and has fine sand to granule size sediment, though the LIBS laser hit an area dominated by medium to coarse sand with sparse very coarse sand (Fig. 5b). Wakham_Bay is moderately to poorly sorted and has medium to very coarse sand with sparse granules; at least one of the points hit a very coarse sand size grain, and another hit a granule (Fig. 5c).

Unlike the upper members of YKB, grains could not be resolved in the RMI images for the majority of the rocks in PH due to their fine grain sizes. Because of this, grain size estimates were primarily based on observations made using MAHLI images, supplemented by the RMI images when applicable. Thus, grain size estimates for most PH rocks do not correspond to the specific ChemCam LIBS scene used for G_{MEAN}. The rocks of Confidence Hills are composed predominantly of grains below the resolution of MAHLI and RMI, but occasional sand-sized grains were discernible in MAHLI images. They represent mud-dominated rocks at PH. The rocks at Alexander Hills are mudstones and have silt to very fine sand sized voids; rare voids were more than a millimeter in diameter (Fig. 6a). The rocks of Book Cliffs and the upper section of Chinle, appear coarser-grained than mudstones observed elsewhere at PH, with

abundant discernible silt- and very fine sand-sized grains observed in MAHLI images. The rocks of the upper Chinle are cross-laminated supporting the presence of sand (Fig. 6b). Medium sand-sized protrusions are also present in the rocks at Book Cliffs, though they may be diagenetic features. These targets are used to define the lower and upper limits of rocks with silt to very fine sand, and the lower limit of rocks with fine sand. The three rock targets at the Whale Rock outcrop are the coarsest rocks analyzed by ChemCam at PH, and grains can be resolved in the RMI images. All Whale Rock targets have very poorly sorted medium to coarse sand with sparse very coarse sand in a matrix of finer sediment not resolved in the RMI or MAHLI images (Fig. 6c). These rocks help define G_{MEAN} values for rocks composed of medium to very coarse sand. The Whale rock outcrop has climbing-ripple cross-stratification supporting the presence of sand (Fig. 6d).

5.2. Calibration of the GIMS to grain size

The GIMS values of rock targets with grain sizes constrained by images were used to calibrate G_{MEAN} to grain size (Table 1). For these targets, the magnitude of G_{MEAN} increased consistently with grain size in both YKB and PH. Mudstones from the Sheepbed member have the lowest mean G_{MEAN}, at 0.04±0.01, with a minimum G_{MEAN} value of 0.02±0.00 and maximum of 0.06±0.00. Whereas the medium to coarse sandstones of the Whale Rock outcrop have the highest mean G_{MEAN} at 0.23±0.05, with a minimum G_{MEAN} value of 0.18±0.01 and maximum of 0.29±0.01. Rocks with intermediate grain sizes have intermediate G_{MEAN} values. Also, rocks with the same grain size have similar G_{MEAN} in both YKB and PH. For example, the target Gillespie_Lake_1 from YKB and Vasquez from PH, have medium to coarse sand sized grains, and have G_{MEAN} values of 0.16±0.00 and 0.18±0.01, respectively. Thus, G_{MEAN} values correlate well with grain sizes constrained from images.

Based on the G_{MEAN} of the standards, four grain size regimes in G_{MEAN} space (GSR1-4) were defined using a similar classification scheme as the Wentworth scale (Wentworth, 1992): clay to silt (G_{MEAN}=0.00-0.07; GSR1), silt to fine sand (G_{MEAN}=0.08-0.11; GSR2), fine to medium sand (G_{MEAN}=0.11-0.14; GSR3), and medium to very coarse sand (G_{MEAN}=0.15-0.29; GSR4). The GSR1, GSR2, and GSR4 bins have multiple calibration standards, and thus their G_{MEAN} ranges are well constrained. The upper and lower G_{MEAN} bounds of these GSRs were defined by using the minimum and maximum G_{MEAN} of the calibration rocks in each bin (Table 1). The lower bound of GSR1 was extended to 0.00 as that is the theoretical minimum for a homogenous rock (see Section 2.2). GSR3, unlike the other bins, is not well constrained because it has only one calibration rock (Nanok; G_{MEAN}=0.11). Because the G_{MEAN} of Nanok overlaps with the upper bound of the pre-defined GSR2 bin, its value was chosen to be the lower bound of GSR3. Rocks with G_{MEAN}=0.11 are exactly at the boundary and are reported as GSR2/GSR3. The upper bound of GSR3 was chosen to be the mid-point distance between the lower bound of GSR3 and that of GSR4. GSR3 is illustrated differently in figures 3, 4, and 8 to highlight its poor calibration.

5.3. Inferred grain sizes using the GIMS

G_{MEAN} was calculated for 50 rocks from YKB and 15 from PH (Table 2). Of the 50 rocks in YKB, 16 are calibration standards, an additional 11 have known grain sizes from image data, and 23 have unknown grain sizes (Table 2). Of the 15 rocks from PH, 11 are calibration standards and 4 have unknown grain sizes (Table 2). All rocks were pre-screened to exclude

significant diagenetic features (see Section 2.2). Grain size ranges for all rocks were then assigned using the regimes from the calibration exercise (see Section 5.2).

At YKB, only the rocks from the Sheepbed member are in GSR1 (Table 2; Fig. 3). Rocks from Gillespie Lake and the Glenelg members are primarily in GSR3 and GSR4 (Table 2; Fig. 3). Thus, there is a discontinuity in the predicted grain sizes of rocks between the Sheepbed mudstone and rest of YKB.

At PH, the grain size regime increases overall with increasing elevation from GSR1 at Confidence Hills to GSR4 at Whale Rock. This increasing upward trend deviates at Chinle where the G_{MEAN} is GSR1 at the base of the outcrop and increases to GSR2/GSR3 at the top. Most GSR4 rocks are in Whale Rock; the exception is Aztec_2 from Alexander Hills.

In general, the Sheepbed mudstones have lower G_{MEAN} than those from Confidence Hills. Apart from one rock target, YKB also appears to be devoid of rocks in GSR2; although three are transitional between GSR2 and GSR3. Thus, at YKB, rocks are either in GSR1 or in GSR3 and 4. The G_{MEAN} of rocks in GSR4 in PH is greater than those in GSR4 at YKB.

Some of the rocks at YKB have multiple LIBS analyses allowing an opportunity to test the reproducibility of the GIMS (Table 2). For example, at Gillespie Lake, the same rock was targeted twice using 3x3 rasters; Gillespie_Lake_1 was taken on the vertical face of the bedrock whereas Gillespie_Lake_2 was taken on the exposed top face. Both are in GSR4 (Fig. 7a). In the Point Lake outcrop, Balboa_Dismal_Lakes and Balboa2, are 3x3 rasters that overlap each other on the vertical face of the same rock and are in GSR3 and GSR2/GSR3, respectively. At the Rocknest outcrop, three rocks were targeted multiple times by the LIBS (Table 2). An example is a float rock that was targeted three times, twice by 1x10 vertical rasters, Rocknest_3a and Rocknest_3b, and once by a 1x5 diagonal raster, Rocknest3 (Fig. 7b). The Rocknest3a and Rocknest3b rasters formed a vertical transect from the bottom to top of the float rock, and are both in GSR4, whereas Rocknest3 was several millimeters to the left and below the previous rasters and is GSR3 (Fig. 7b).

5.4. Validation of GIMS results to grain size from images

For all rocks with known grain size, their G_{MEAN} values were compared to the grain sizes measured from images (Fig. 8). Overall, G_{MEAN} increases with increasing grain size for rocks with mud to medium sand from 0.00-0.13 (Fig. 8). For rocks with medium sand to very fine gravel, G_{MEAN} varies between 0.15-0.29, and there are no apparent trends with grain size with increasing G_{MEAN} (Fig. 8).

The predicted GSRs of rocks are consistent with their grain size constrained from images (Fig. 8). All rocks composed of mud to very fine sand based on image data are calibration standards and are in GSR1 and GSR2 bins. Three rocks with known grain size are in GSR3, including the GSR3 calibration standard. The other two rocks in GSR3 have fine to medium sand, although one also has at least some coarse sand. All three GSR3 rocks have <5-10% resolvable grains in the RMI images, making visual grain size estimates biased toward coarser grains or those with more contrast. For the GSR4 bin, in addition to the four standards, there are ten other rocks with resolvable grains in images, and these all have grains that are coarser than medium sand. Out of the ten, three have <5-10% resolvable grains in the RMI images. Most of the GSR4 rocks are poorly to very poorly sorted based on visual grain size estimations.

6. Discussion

6.1. GIMS as a proxy for grain size

553 The GIMS is a robust technique for inferring grain size differences in the rocks from
554 YKB and PH across regional and compositional differences. At both locations, mudstones have
555 the smallest G_{MEAN} and medium to coarse sandstones have the largest G_{MEAN} (Fig. 3, Fig. 4, Fig.
556 8; Table 2). GSRs were calibrated to a select number of rock standards and validated by applying
557 the GIMS to other rocks with known grain size (Fig. 8). The predicted GSRs of rocks not used in
558 the calibration are consistent with their grain size constrained from images (Fig. 8).
559 Overall, the GIMS successfully predicts the grain size of rocks of known grain size (Fig.
560 3, Fig. 4, Fig. 8). In our dataset, the GIMS is particularly sensitive when rocks have grains
561 smaller than medium sand and $G_{MEAN}<0.15$ (Fig. 8), because G_{MEAN} increases with increasing
562 grain size. However, when rocks have grains that are medium sand to granule in size, the G_{MEAN}
563 rolls off instead of continuing to increase with grain size because medium sand to granule sized
564 grains are all larger than the LIBS spot size; each LIBS spot samples only one or two grains (Fig.
565 2; Section 2.2). Theoretically, rocks with grains up to the size of the LIBS spot spacing, typically
566 5 mm, would produce similar G_{MEAN} values. Thus, rocks with grains ranging from medium sand
567 to fine gravel in size could cause the same magnitude of variability from point-to-point and thus
568 be part of GSR4. This insensitivity of G_{MEAN} to grain size explains the large bin size for GSR4
569 compared to the other bins.
570 The ChemCam LIBS targeted some rocks more than once, allowing an opportunity to
571 investigate the reproducibility of the GIMS (e.g., Fig. 7; Table 2). Commonly, the G_{MEAN} of the
572 analyses are similar, with values falling within 0.03 of each other, placing them in the same GSR
573 (Table 2). Results are particularly consistent for the rocks at PH and the Sheepbed member of
574 YKB. However, GSRs predicted by the GIMS are variable for rocks in the Gillespie Lake and
575 Glenelg members at YKB. Rocks from both members are predominantly poorly sorted and some
576 are matrix supported (Grotzinger et al., 2014; 2015; Mangold et al., 2015; Anderson et al., 2015;
577 Edgar et al., 2017). Since the GIMS is a statistical technique, if the LIBS analysis preferentially
578 samples a subset of grain sizes, the analysis will not represent the rock or unit as a whole. This
579 was the case for Gillespie_Lake_1, which is in a rock that has fine sand to medium gravel sized
580 grains (Grotzinger et al., 2014; Mangold et al., 2015), but medium to coarse sand near the laser
581 pits of the LIBS analysis (Fig. 5b). The GSR prediction of GSR4 for Gillespie_Lake_1 is
582 consistent with the grain sizes sampled by LIBS, but not the rock as a whole. The variability in
583 G_{MEAN} between analyses on the same rock can be used to suggest poor sorting, or the data can be
584 evaluated to see how many analyses are necessary to obtain a rigorous grain size prediction.
585 Thus, to obtain a meaningful GRS prediction, significantly more data are required for poorly
586 sorted or heterogeneous rocks than for ones with grains of uniform size. It is possible that the
587 variability between some GSRs for the same rock is due to the poor calibration of the GSR3 bin.
588 One of the Rocknest float rocks (Fig. 7b) has two analyses in GSR4 with $G_{MEAN}=0.15$ and 0.16,
589 and one in GSR3 with a $G_{MEAN}=0.13$ (Table 2). Grain sizes were not resolved in this rock from
590 image data. The variable GSR prediction may reflect either grain size variations or the poor
591 calibration of the GSR3 bin. It is possible that the GSR3 bin spans a narrower range of G_{MEAN},
592 and that the GSR4 bin extends to lower values, as there are no rocks with G_{MEAN} from 0.13-0.15
593 with known grain size in our dataset.
594 One outcrop shows an inconsistency between the GSR inferred and image analysis. At
595 PH, the Alexander Hills outcrop has a higher inferred GSR than is interpreted from image data.
596 Clastic grains could not be resolved in the MAHLI images of rocks in this outcrop, suggesting
597 that it is dominated by mud, but the G_{MEAN} results suggest a grain size of fine to medium sand.
598 Voids ranging in size from silt/very fine sand to very coarse sand were resolved in images (Fig.

6a). These observations suggest that this outcrop either is a sandstone, or that there are unresolved diagenetic features present in the rock that increased compositional heterogeneity and thus led to a higher predicted GSR.

Variability in G_{MEAN} can arise from factors in addition to grain size and sorting. Rocks with grains that have a small range in composition will have low point-to-point variability and a low G_{MEAN} irrespective of grain size, whereas rocks with grains of diverse compositions will have high point-to-point variability and higher G_{MEAN} for a given grain size. Martian sedimentary rocks are generally expected to have a diverse suite of grain compositions, because Mars, unlike Earth, is mostly basaltic, with sediment grains consisting of pyroxene, feldspar, olivine, other mafic minerals, and glass. Basaltic minerals are the most abundant minerals present at YKB and PH based on ChemCam and the CheMin analyses (Sautter et al., 2014; Vaniman et al., 2013; Mangold et al., 2016; Cousin et al., 2017; Rampe et al., 2017). Even aeolian dunes, which are normally dominated by quartz on Earth, are composed of basaltic minerals on Mars (Lapotre et al., 2017). Because the GIMS is very sensitive to grain compositions, calibration relative to sampled compositions is critical for GSR predictions to be meaningful. To account for compositional variability between rocks, the major-element oxides for all rocks must be normalized together before calculating G_{MEAN} (see Appendix). This calibration takes into account that some oxides, such as CaO and MgO, vary more in magnitude between samples than other oxides, such as SiO_2 (see Section 3.2). The element variability normalization ensures that the contribution from each oxide to the overall variability of a rock is weighted to make the GIMS sensitive to grain size variations. If the LIBS data were not normalized, the G_{MEAN} of rocks would depend on both compositional variations and grain size, and the use of the GIMS would predict inaccurate grain sizes. Because of this need for compositional calibration, the calibration of G_{MEAN} to GSR presented in this manuscript is not directly comparable to results of past studies that have used the Gini index (e.g., Mangold et al., 2017) or future studies that use the GIMS without renormalization of the compositions.

Due to the sensitivity of the GIMS to compositional variations, G_{MEAN} can also be biased on rocks with a high proportion of diagenetic phases. LIBS spots might include variable proportions of diagenetic phases, making the heterogeneity higher or lower than that produced by grain size alone. This would be the case for coarse rocks with intra-granular cements, as the laser may hit different proportions of cement and grain at each spot. Since coarser grained rocks have more pore space to accommodate cements, contributions from cements may increase with increasing grain size. For rocks with grains smaller than the laser spot size (medium sand), this would provide a component with a consistent composition from point to point, and would not affect G_{MEAN}. For rocks with grains about the size or coarser than the laser spot size, the LIBS may sample cement in some raster points at grain boundaries, providing a variable contribution that could potentially increase G_{MEAN}. Thus, rocks with medium sand may end up in GSR4 rather than GSR3, whereas rocks with grains coarser than medium sand would remain in GSR4, due to the roll off in G_{MEAN} with increasing grain size (see above). Rocks that are poorly sorted would accommodate less cements than those that are better sorted and would be less affected by the cement contribution. Regardless of grain size and sorting, if the composition of the cement includes elements that are not one of the major-element oxides detected by ChemCam (e.g., SO_4 cement), then the filtering process would remove points with high cement contributions based on their sum of oxides. In contrast, the filtering process would not remove points with cement contributions that have compositions similar to the host rock.

644 Similarly, diagenetic features such as concretions can cause variability. Sand sized dark
645 features, possibly micro-diagenetic concretions, are pervasive in rocks from Pink Cliffs,
646 Shoemaker, Book Cliffs, and Telegraph Peak, and may be present at Alexander Hills. As these
647 features are of the same scale as the LIBS spot, they would have caused variations consistent
648 with sand. Differentiating between heterogeneities due to diagenetic contributions and grain size
649 may be difficult when both are not resolvable or distinguishable in image data. However, more
650 detailed analyses can improve interpretations. If variability is due to grain size, most major-
651 element oxides should vary, whereas only certain oxides will vary for diagenetic contributions
652 (e.g., Nachon et al., 2017). For example, high CaO is associated with $CaSO_4$ cement; when
653 $CaSO_4$ is sampled, CaO is high with all other oxides showing a reduced contribution (e.g.,
654 Nachon et al., 2017).
655 Where grains and diagenetic features cannot be distinguished, interpretations can be
656 challenging. It is possible that chemical variability in rocks inferred to be in GSR2 could be due
657 to diagenetic contributions and not grain size. Such an interpretation is difficult to test when
658 sand or coarse silt cannot be verified in images and sedimentary structures associated with sand,
659 such as cross-bedding, are not present. Silt to fine sand grain sizes are at or below the boundary
660 of resolution for all of the cameras on the rover, and it is difficult to confirm visually the
661 presence of grains in this size range. This grain size is also below the minimum LIBS laser spot
662 size. However, for this study, the only rocks in GSR2 with known grain size are in the upper
663 Chinle outcrop, which shows cross-bedding (Fig. 4b; see Section 6.2). The sedimentary
664 structures support the GSR interpretation that there is sand present in these rocks. Several rocks
665 from YKB with unknown grain size have G_{MEAN} that straddle the GSR2 and GSR3 bins. Due to
666 their unknown grain size, it is uncertain whether their G_{MEAN} reflect grain size or the poor
667 calibration of the boundaries for GSR3. The transition between GSR1 and GSR2 is important, as
668 it may represent a change in flow regime for the sediments. GSR1 grain sizes are associated with
669 suspended load transport and those of GSR2 with bedload (traction) transport.
670 Due to the statistical nature of the GIMS, G_{MEAN} also depends on the size of LIBS
671 analysis spots and the spacing between these spots. The size of LIBS spots varies with rock
672 hardness and distance between ChemCam and the rock (e.g., Maurice et al., 2012b), producing
673 different analysis areas between observations. Each LIBS point covers a smaller area and thus
674 fewer grains for short distance analyses versus long distance ones. Thus, it is predicted that
675 sandstones with grain sizes on the order of LIBS spot sizes or smaller could show greater
676 heterogeneity at shorter distances than longer ones. In contrast, rocks with mud-sized grains will
677 consistently have little to no point-to-point heterogeneities because LIBS spots are always large
678 enough to analyze a statistically significant number of grains. LIBS spot size and shape is also
679 affected by rock hardness (Arvidson et al., 2014), which may produce minor variations in GIMS
680 results. For rocks in our dataset with known grain size, distances from the rover varied
681 (Supplemental Table 1) but no effects from grain size were identified. Based on the calibration
682 data and evaluation, it appears that variations in the laser spot size are smaller than the breadth of
683 the defined GSR and can be accounted for with detailed analysis of spot sizes if called for in
684 future analyses.
685 In this study, the GSRs inferred from G_{MEAN} generally correlate very well with the grain
686 sizes observed in images where data is available. Thus, G_{MEAN} provides an excellent estimate of
687 grain size ranges for rocks lacking visible diagenetic features. For future studies using the GIMS,
688 the accuracy of the predicted GSRs can be increased if more rocks with known grain size are
689 calibrated to G_{MEAN}. This requires complimentary targeting of rocks with both MAHLI and

ChemCam in multiple regions along *Curiosity's* traverse, to be able to tie together detailed grain size information with point-to-point variabilities in ChemCam LIBS data. Rocks with fine to medium sand grains are particularly important to characterize as these are needed to constrain the extent of the GSR3 bin.

6.2. New insights into depositional environments of Yellowknife Bay and Pahrump Hills

Vertical Trends in Stratigraphy

The grain sizes at YKB are heterogeneous within the stratigraphic column (Fig. 3, Fig. 8). The discontinuity in grain size between the Sheepbed mudstone and rest of YKB sedimentary rocks demonstrate that flow characteristics shifted abruptly between accumulation of the Sheepbed mudstone and deposition of the overlying poorly sorted sandstones. The grain size of rocks at Point Lake and Rocknest outcrops previously were not well constrained from image data. For Point Lake, the mean G_{MEAN} is at the upper end of the fine to medium sand size range, with the majority of the rocks in GSR3 and GSR4. The variability of the G_{MEAN} between targets suggests that Point Lake rocks are poorly sorted. For Rocknest, the mean G_{MEAN} is at the lower end of the medium to very coarse sand size range, with the majority of the rocks in GSR4. Thus, the Rocknest outcrop is likely dominated by grains of medium sand and coarser. The lack of variability between the analyses suggests that the rocks are better sorted than those of Point Lake. Overall, the grain size variations at YKB are heterogeneous within the stratigraphic column (Fig. 3, Fig. 8), and the lack of rocks in GSR2 suggests bimodal flow conditions in the depositional environment. These results were consistent with deposition in an alluvial environment with a lake (Grotzinger et al., 2014).

At PH, there is a progressive increase in G_{MEAN} from mud to coarse sand through time (Fig. 4, Fig. 8), which supports prior interpretations that the PH sequence records progradation within a lacustrine depositional setting (Grotzinger et al., 2015; Stack et al., 2016). The overall trend is interrupted at Chinle, where grain sizes varied on the decimeter scale. The Chinle outcrop coarsens upward, and G_{MEAN} increases stratigraphically from mud to very fine to fine sand. From image data, the distribution and grain size of sand were difficult to constrain, but the presence of sand was inferred from cross-stratification in the outcrop (Fig. 6b). The G_{MEAN} results show that the outcrop coarsens upward, which is consistent with increasing average flow speed through time. The accumulation of sediment, however, required that the instantaneous flow was slowing down at this location, which is consistent with deposition in a near-shore environment with a proximal fluvial influx of sediment. This interpretation fits the overall interpretation that the PH region accumulated as part of a delta.

Mudstone Variations

The mudstones at YKB and PH have similar mean G_{MEAN} values, but the ranges of G_{MEAN} values are different. The mudstones of the Sheepbed (YKB) have much lower minimum values than those from Confidence Hills (PH), and Confidence Hills has one rock at the upper end of GSR1. The high G_{MEAN} values suggest that the rocks at Confidence Hills may include coarse silt and potentially dispersed sand grains. In contrast, the finer grain sizes of the Sheepbed member may be due to: 1) alteration and formation of clay minerals, as observed in drill analyses (Vaniman et al., 2013), which homogenized the chemical composition, or 2) a depositional environment with the accumulation of only the finest grain sizes.

7. Concluding Remarks

Overall, the GIMS provides a rigorous method for estimating grain size from chemical heterogeneities in ChemCam LIBS data. Its application requires a careful evaluation of the distribution and characteristics of available LIBS data that is tested against calibration images of rocks with known grain size. The calibration also includes the element variability normalization of all the LIBS data, to account for regional variations of major-element oxide weight fractions (see Appendix). All of the calibration steps are proposed as a standard procedure to use the GIMS, and they were validated by applying the GIMS to sedimentary rocks of various grain sizes from YKB and PH in Gale crater (Table 2; Fig. 8).

By providing grain size predictions, the GIMS expands the current use of the ChemCam LIBS instrument on the *Curiosity* rover. If used appropriately, the GIMS may be used to re-evaluate image-based grain size measurements and provide grain size constraints for regions in Gale crater that have incomplete textural information. The grain sizes inferred from the GIMS are complimentary to those determined from image data and together both techniques can be used to improve interpretations of the depositional environments of rocks analyzed by *Curiosity* and future Mars missions with LIBS, such as the Mars 2020 rover (Maurice et al., 2015; Wiens et al., 2017). Constraining the grain size of martian sedimentary rocks is crucial for interpreting ancient depositional environments and habitability of early Mars.

8. Appendix: Calculating Gini index mean scores from ChemCam LIBS data

The variability of each major-element oxide that ChemCam can detect goes into the GIMS calculation. The compositional ranges of major-element oxides need to be normalized to properly capture grain-size related variability. For example, oxide variations in quartzites are very different than those in basaltic sandstones. By normalizing oxide variations based on the total variability in the suite of rocks analyzed, the Gini mean score will be sensitive to changes in grain size. However, if rocks from regions with two distinctly different compositions are normalized together, the high variability across the sample suite can skew the variability caused by grain size. Thus, to calculate a meaningful Gini mean score, the weight percent range of each oxide within the sample suite must be known *a priori*, compositions should have a moderately narrow range, and the full range of oxides should be used in the normalization. The weight percent of each major-element oxide is normalized from 0 to 1 using *Equation 1*:

$$z_{i,j} = \frac{x_{i,j} - min(x_i)}{max(x_i) - min(x_i)}, \quad (1)$$

where $z_{i,j}$ is the normalized weight percent for point j, and oxide i, and $x_{i,j}$ is the oxide weight percent calculated from LIBS spectra. For any given target, the normalized weight percent values for each oxide are then binned using the same bin size. For this study, the bin size was set by averaging together the mean of 1/5 of the standard deviation for each oxide. The percentage of points per bin relative to the total number of points, *P*, is calculated. The sums of $z_{i,j}$ in each bin and for the entire sample set are calculated, and the percent oxide sum for each bin, *S*, is tabulated. For each target and oxide, *P* is plotted in the x-axis and *S* in the y-axis to determine the Lorenz curve of the data set. The Gini index for each oxide is,

$$G_i = 1 - 2B_i, \quad (2)$$

where B_i is the area under the Lorenz curve for oxide *i*. The area can be calculated using a trapezoidal approximation. To obtain an overall homogeneity parameter, 7 major oxides were

780 averaged using an arithmetic mean to calculate an average G_{ave}. The maximum value that G_{ave}
781 can have depends on the number of points, *N*, per target, where

782 $$G_N = \frac{(N-1)}{N} \quad (3)$$

783 (Mangold et al., 2017). To compensate for this variability, G_N for each target is used to
784 normalize G_{ave},
785

786 $$G_{MEAN} = \frac{G_{ave}}{G_N} \; . \; (3)$$

787
788 G_{MEAN}, the Gini mean score, can then be used to calibrate grain size ranges for the specific suite
789 of samples being studied.
790 Discretion is needed when applying the GIMS, including filtering of data to use, choice
791 of oxides to include, and bin size. In this study, some rock targets were excluded for the GIMS
792 analysis primarily due to the presence or suspected presence of diagenetic features. Contributions
793 from diagenetic features were suspected when the LIBS sum of oxides value was low, suggesting
794 the presence of sulfates, chlorides, or other non-oxide minerals. Analysis of the sum of oxides
795 versus the weight percent of CaO and MgO (oxides commonly associated with diagenesis) of
796 different rock targets from YKB and PH suggested a conservative minimum threshold value of
797 87% for the sum of oxides, and this value was picked for the GIMS analysis presented here. This
798 threshold value should be evaluated for each suite of rocks that are being analyzed with the
799 GIMS. Similarly, different sample suites may require the inclusion or exclusion of specific
800 oxides. For this study, TiO_2 was not included as a major oxide because it has low to no
801 variability in most of the rock targets. However, when it does vary, the magnitude of variation is
802 really high, skewing the G_{MEAN} values for some targets. The exclusion of TiO_2 led to a
803 significantly better grain size calibration. Finally, the bin size chosen for calculating G_i should
804 depend on the purpose of the study. The bin size used in this study was chosen to provide good
805 coverage of the observed grain sizes, which spanned from mud to gravel (see above). However,
806 the appropriate bin size depends on the question being asked. For example, characterizing
807 variability within mudstones and siltstones may require a finer bin size then used in this study
808 (e.g., more bins), to pick out subtle point-to-point chemical variabilities.
809

810 **9. Acknowledgements**

811 This research was funded by the Mars Science Laboratory Project through the NASA
812 Mars Exploration Program and the Centre National d'Etudes Spatiales, France. Rivera-
813 Hernandez was funded by the Chateaubriand STEM Fellowship sponsored by the Embassy of
814 France in the United States. We are grateful to the MAHLI, Mastcam, and ChemCam teams for
815 providing outstanding data on which to base this research. In particular, Rivera-Hernandez
816 would like to thank the ChemCam science team for welcoming her to the team and providing
817 constructive conversations on how to use, interpret, and access the ChemCam data.
818

819 **10. References**

820 Anderson, R.B. & Bell III, J. F. (2010). Geologic mapping and characterization of Gale Crater
821 and implications for its potential as a Mars Science Laboratory landing site. *Mars* 5, pp.
822 76-128.
823 Anderson, R.B., Morris, R.V., Clegg, S.M., Bell, J.F., Wiens, R.C., Humphries, S.D.,
824 Mertzman, S.A., Graff, T.G. and McInroy, R. (2011). The influence of multivariate

825 analysis methods and target grain size on the accuracy of remote quantitative chemical
826 analysis of rocks using laser induced breakdown spectroscopy. *Icarus*, *215*(2), pp.608-
827 627.
828 Anderson, R., Bridges, J.C., Williams, A., Edgar, L., Ollila, A., Williams, J., Nachon, M.,
829 Mangold, N., Fisk, M., Schieber, J. and Gupta, S. (2015). ChemCam results from the
830 Shaler outcrop in Gale crater, Mars. *Icarus*, *249*, 2-21.
831 Anderson, D.E., Ehlmann, B.L., Forni, O., Clegg, S.M., Cousin, A., Thomas, N.H., Lasue, J.,
832 Delapp, D.M., McInroy, R.E., Gasnault, O. and Dyar, M.D. (2017). Characterization of
833 Laser-Induced Breakdown Spectroscopy (LIBS) emission lines for the identification of
834 chlorides, carbonates, and sulfates in salt/basalt mixtures for the application to MSL
835 ChemCam data. *Journal of Geophysical Research: Planets*.
836 Arvidson, R. E., Bellutta, P., Calef, F., Fraeman, A. A., Garvin, J. B., Gasnault, O., Grant, J. A.,
837 Grotzinger, J. P., Hamilton, V. E., Heverly, M., Iagnemma, K. A., Johnson, J. R., Lanza,
838 N., LeMouélic, S., Mangold, N., Ming, D. W., Mehta, M., Morris, R. V., Newsom, H. E.,
839 Rennó, N., Rubin, D., Schieber, J., Sletten, R., Stein, N. T., Thuillier, F., Vasavada, A.
840 R., Vizcaino, J., and Wiens, R. C. (2014). Terrain physical properties derived from
841 orbital data and the first 360 sols of Mars Science Laboratory Curiosity rover
842 observations in Gale Crater. *Journal of Geophysical Research: Planets*, *119*(6), pp.1322-
843 1344.
844 Banham, S. G., Gupta, S., Rubin, D.M., Watkins, J.A., Sumner, D.Y., Edgett, K.S., Grotzinger,
845 J.P., Lewis, K.W., Edgar, L.A., Stack-Morgan, K.M., Barnes, R., Bell III, J.F., Day,
846 M.D., Ewing, R.C., Lapotre, M.P.A, Stein, N.T., Rivera-Hernández, F., Vasavada, A.R.
847 (2018) Sedimentology of an Ancient Aeolian Sandstone in the Lower Slope of Aeolis
848 Mons, Stimson Formation, Gale Crater, Mars, *Sedimentology*.
849 Bell, J.F., Godber, A., McNair, S., Caplinger, M.A., Maki, J.N., Lemmon, M.T., Van Beek, J.,
850 Malin, M.C., Wellington, D., Kinch, K.M. and Madsen, M.B. (2017). The Mars Science
851 Laboratory Curiosity Rover Mast Camera (Mastcam) Instruments: Pre-Flight and
852 In-Flight Calibration, Validation, and Data Archiving. *Earth and Space Science*.
853 Blaney, D.L., Wiens, R.C., Maurice, S., Clegg, S.M., Anderson, R.B., Kah, L.C., Le Mouélic,
854 S., Ollila, A., Bridges, N., Tokar, R. and Berger, G. (2014). Chemistry and texture of the
855 rocks at Rocknest, Gale Crater: Evidence for sedimentary origin and diagenetic
856 alteration. *Journal of Geophysical Research: Planets*, *119*(9), pp.2109-2131.
857 Clegg, S. M., Sklute, E., Dyar, M. D., Barefield, J. E., & Wiens, R. C. (2009). Multivariate
858 analysis of remote laser-induced breakdown spectroscopy spectra using partial least
859 squares, principal component analysis, and related techniques. Spectrochimica Acta Part
860 B: Atomic Spectroscopy, 64(1), 79-88.
861 Clegg, S.M., Wiens, R.C., Anderson, R., Forni, O., Frydenvang, J., Lasue, J., Cousin, A., Payré,
862 V., Boucher, T., Dyar, M.D. and McLennan, S.M. (2017). Recalibration of the Mars
863 Science Laboratory ChemCam instrument with an expanded geochemical
864 database. *Spectrochimica Acta Part B: Atomic Spectroscopy*, *129*, pp.64-85.
865 Cousin, A., Forni, O., Maurice, S., Gasnault, O., Fabre, C., Sautter, V., Wiens, R.C. and
866 Mazoyer, J. (2011). Laser induced breakdown spectroscopy library for the Martian
867 environment. *Spectrochimica Acta Part B: Atomic Spectroscopy*, *66*(11), pp.805-814.
868 Cousin, A., Sautter, V., Payré, V., Forni, O., Mangold, N., Gasnault, O., Le Deit, L., Johnson,
869 J., Maurice, S., Salvatore, M. and Wiens, R.C. (2017). Classification of igneous rocks
870 analyzed by ChemCam at Gale crater, Mars. *Icarus*, *288*, pp.265-283.

871 Cremers D.A. and Radziemski L.J. (2013) Handbook of Laser-Induced Breakdown
872 Spectroscopy, 2nd Edition, Wiley, doi: 10.1002/9781118567371.
873 Edgar, L.A., Gupta, S., Rubin, D.M., Lewis, K.W., Kocurek, G.A., Anderson, R.B., Bell, J.F.,
874 Dromart, G., Edgett, K.S., Grotzinger, J.P. and Hardgrove, C. (2017). Shaler: In situ
875 analysis of a fluvial sedimentary deposit on Mars. *Sedimentology*.
876 Edgett, K.S., Yingst, R.A., Ravine, M.A., Caplinger, M.A., Maki, J.N., Ghaemi, F.T.,
877 Schaffner, J.A., Bell, J.F., Edwards, L.J., Herkenhoff, K.E. and Heydari, E. (2012).
878 Curiosity's Mars hand lens imager (MAHLI) investigation. *Space science reviews*, *170*(1-
879 4), pp.259-317.
880 Edgett, K.S., Caplinger, M.A., Maki, J.N., Ravine, M.A., Ghaemi, F.T., McNair, S.,
881 Herkenhoff, K.E., Duston, B.M., Willson, R.G., Yingst, R.A. and Kennedy, M.R.
882 (2015). *Curiosity's robotic arm-mounted Mars Hand Lens Imager (MAHLI):*
883 *Characterization and calibration status* (Vol. 1, No. 19, p. 2). MSL MAHLI Technical
884 Report.
885 Fabre, C., S. Maurice, A. Cousin, R. C. Wiens, O. Forni, V. Sautter, and D. Guillaume.
886 "Onboard calibration igneous targets for the Mars Science Laboratory Curiosity rover and
887 the Chemistry Camera laser induced breakdown spectroscopy
888 instrument." *Spectrochimica Acta Part B: Atomic Spectroscopy* 66, no. 3 (2011): 280-
889 289.
890 Farmer, J. D., & Des Marais, D. J. (1999). Exploring for a record of ancient Martian
891 life. *Journal of Geophysical Research: Planets*, *104*(E11), 26977-26995.
892 Fraeman, A.A., Arvidson, R.E., Catalano, J.G., Grotzinger, J.P., Morris, R.V., Murchie, S.L.,
893 Stack, K.M., Humm, D.C., McGovern, J.A., Seelos, F.P. and Seelos, K.D. (2013). A
894 hematite-bearing layer in Gale Crater, Mars: Mapping and implications for past aqueous
895 conditions. *Geology*, *41*(10), pp.1103-1106.
896 Fraeman, A.A., Ehlmann, B.L., Arvidson, R.E., Edwards, C.S., Grotzinger, J.P., Milliken, R.E.,
897 Quinn, D.P. and Rice, M.S. (2016). The stratigraphy and evolution of lower Mount Sharp
898 from spectral, morphological, and thermophysical orbital data sets. *Journal of*
899 *Geophysical Research: Planets*, *121*(9), pp.1713-1736.
900 Jackson, R. S. (2016). Investigation of Aqueous Processes in the Valle Grande Paleo-Lake,
901 Valles Caldera as a Martian Analog; Chemcam Investigation of the John Klein and
902 Cumberland Drill Holes and Tailings, Gale Crater, Mars (master's thesis). University of
903 New Mexico, Albuquerque, New Mexico.
904 Kah, L.C., Kronyak, R., Van Beek, J., Nachon, M., Mangold, N., Thompson, L., Wiens, R.,
905 Grotzinger, J., Farmer, J., Minitti, M. and Shieber, J. (2015). Diagenetic crystal clusters
906 and dendrites, lower Mount Sharp, Gale Crater.
907 Kronyak, R.E., Kah, L.C., Nachon, M., Mangold, N., Weins, R.C., Williams, R., Schieber, J.
908 and Grotzinger, J. (2015, March). Distribution of mineralized veins from Yellowknife
909 Bay to Mount Sharp, Gale Crater, Mars: Insight from textural and compositional
910 variation. In *Abstract 1903 presented at Lunar and Planet. Sci. Conf* (Vol. 46).
911 Gini, C. (1921). Measurement of inequality of incomes. *The Economic Journal*, *31*(121),
912 pp.124-126.
913 Grant, J.A., Wilson, S.A., Mangold, N., Calef, F. and Grotzinger, J.P. (2014). The timing of
914 alluvial activity in Gale crater, Mars. *Geophysical Research Letters*, *41*(4), pp.1142-1149.
915 Grotzinger, J. P., Crisp, J., Vasavada, A. R., Anderson, R. C., et al. (2012). Mars Science
916 Laboratory mission and science investigation. *Space science reviews*, *170*(1-4), 5-56.

Grotzinger, J.P., Sumner, D.Y., Kah, L.C., Stack, K., Gupta, S., Edgar, L., Rubin, D., Lewis, K., Schieber, J., Mangold, N. and Milliken, R. (2014). A habitable fluvio-lacustrine environment at Yellowknife Bay, Gale Crater, Mars. *Science*, *343*(6169), p.1242777.

Grotzinger, J. P., Gupta, S., Malin, M. C., Rubin, D. M., Schieber, J., Siebach, K., et al. (2015). Deposition, exhumation, and paleoclimate of an ancient lake deposit, Gale crater, Mars. Science, 350(6257), aac7575.

Lasue, J., Mangold, N., Cousin, A., Meslin, P.Y., Wiens, R., Gasnault, O., Rapin, W., Schroder, S., Ollila, A., Fabre, C. and Berger, G. (2016, October). ChemCam analysis of martian fine dust. In *AAS/Division for Planetary Sciences Meeting Abstracts* (Vol. 48).

Le Deit, L., Hauber, E., Fueten, F., Pondrelli, M., Rossi, A.P. and Jaumann, R. (2013). Sequence of infilling events in Gale Crater, Mars: Results from morphology, stratigraphy, and mineralogy. *Journal of Geophysical Research: Planets*, *118*(12), pp.2439-2473.\

Le Mouélic, S., Gasnault, O., Herkenhoff, K.E., Bridges, N.T., Langevin, Y., Mangold, N., Maurice, S., Wiens, R.C., Pinet, P., Newsom, H.E. and Deen, R.G. (2015). The ChemCam Remote Micro-Imager at Gale crater: Review of the first year of operations on Mars. *Icarus*, *249*, pp.93-107.

Leveille, R.J., Bridges, J., Wiens, R.C., Mangold, N., Cousin, A., Lanza, N., Forni, O., Ollila, A., Grotzinger, J., Clegg, S. and Siebach, K. (2014). Chemistry of fracture-filling raised ridges in Yellowknife Bay, Gale Crater: Window into past aqueous activity and habitability on Mars. *Journal of Geophysical Research: Planets*, *119*(11), pp.2398-2415.

Malin, M.C. and Edgett, K.S., 2000. Sedimentary rocks of early Mars. *Science*, *290*(5498), pp.1927-1937.

Malin, M.C., Ravine, M.A., Caplinger, M.A., Ghaemi, F.T., Schaffner, J.A., Maki, J.N., Bell, J.F., Cameron, J.F., Dietrich, W.E., Edgett, K.S. and Edwards, L.J. (2016). The Mars Science Laboratory (MSL) Mast cameras and Descent imager: I. Investigation and instrument descriptions. *Earth and Space Science*.

Mangold, N., Forni, O., Dromart, G., Stack, K., Wiens, R.C., Gasnault, O., Sumner, D.Y., Nachon, M., Meslin, P.Y., Anderson, R.B. and Barraclough, B. (2015). Chemical variations in Yellowknife Bay formation sedimentary rocks analyzed by ChemCam on board the Curiosity rover on Mars. *Journal of Geophysical Research: Planets*, *120*(3), pp.452-482.

Mangold, N., Thompson, L.M., Forni, O., Williams, A.J., Fabre, C., Le Deit, L., Wiens, R.C., Williams, R., Anderson, R.B., Blaney, D.L. and Calef, F. (2016). Composition of conglomerates analyzed by the Curiosity rover: Implications for Gale Crater crust and sediment sources. *Journal of Geophysical Research: Planets*, *121*(3), pp.353-387.

Mangold, N., Schmidt, M. E., Fisk, M. R., Forni, O., McLennan, S. M., Ming, D. W., Sautter, V., Sumner, D., et al. (2017). Classification scheme for sedimentary and igneous rocks in Gale crater, Mars. *Icarus*, *284*, 1-17.

Maurice, S., Wiens, R. C., Saccoccio, M., Barraclough, B., Gasnault, O., Forni, O., et al. (2012a). The ChemCam instrument suite on the Mars Science Laboratory (MSL) rover: Science objectives and mast unit description. Space science reviews, 170(1-4), 95-166.

Maurice, S., Cousin, A., Wiens, R.C., Gasnault, O., Parès, L., Forni, O., Meslin, P.Y., Clegg, S. and Team, C. (2012b), March. Laser Induced Breakdown Spectroscopy (LIBS) spot size at Stand-off distances with ChemCam. In *Lunar and Planetary Science Conference* (Vol. 43).

962 Maurice, S., Wiens, R.C., Anderson, R., Beyssac, O., Bonal, L., Clegg, S., DeFlores, L.,
963 Dromart, G., Fischer, W., Forni, O. and Gasnault, O. (2015, March). Science objectives
964 of the SuperCam instrument for the Mars2020 rover. In *Lunar and Planetary Science*
965 *Conference* (Vol. 46, p. 2818).
966 McCanta, M. C., Dobosh, P. A., Dyar, M. D., & Newsom, H. E. (2013). Testing the veracity of
967 LIBS analyses on Mars using the LIBSSIM program. *Planetary and Space Science*, *81*,
968 48-54.
969 McCanta, M.C., Dyar, M.D., Dobosh, P.A., Davidson, G.R., Hill, C.A., Wolgemuth, K.,
970 Romanowicz, B., Hirschmann, M., Kellogg, L., Manga, M. and Mukhopadhyay, S.
971 (2017). Extracting Bulk Rock Properties from Microscale Measurements: Subsampling
972 and Analytical Guidelines. *GSA Today*, *27*(7).
973 McLennan, S. M. (2012). Geochemistry of sedimentary processes on Mars. *Sedimentary*
974 *Geology of Mars*, *102*, 119-138.
975 McLennan, S.M., Anderson, R.B., Bell, J.F., Bridges, J.C., Calef, F., Campbell, J.L., Clark,
976 B.C., Clegg, S., Conrad, P., Cousin, A. and Des Marais, D.J. (2014). Elemental
977 geochemistry of sedimentary rocks at Yellowknife Bay, Gale crater,
978 Mars. *Science*, *343*(6169), p.1244734.
979 Milliken, R.E., Grotzinger, J.P. and Thomson, B.J. (2010). Paleoclimate of Mars as captured by
980 the stratigraphic record in Gale Crater. *Geophysical Research Letters*, *37*(4).
981 Ming, D.W., Archer, P.D., Glavin, D.P., Eigenbrode, J.L., Franz, H.B., Sutter, B., Brunner,
982 A.E., Stern, J.C., Freissinet, C., McAdam, A.C. and Mahaffy, P.R. (2014). Volatile and
983 organic compositions of sedimentary rocks in Yellowknife Bay, Gale Crater,
984 Mars. *Science*, *343*(6169), p.1245267.
985 Nachon, M., Clegg, S.M., Mangold, N., Schröder, S., Kah, L.C., Dromart, G., Ollila, A.,
986 Johnson, J.R., Oehler, D.Z., Bridges, J.C. and Le Mouélic, S. (2014). Calcium sulfate
987 veins characterized by ChemCam/Curiosity at Gale crater, Mars. *Journal of Geophysical*
988 *Research: Planets*, *119*(9), pp.1991-2016.
989 Nachon, M., Mangold, N., Forni, O., Kah, L.C., Cousin, A., Wiens, R.C., Anderson, R., Blaney,
990 D., Blank, J.G., Calef, F. and Clegg, S.M. (2017). Chemistry of diagenetic features
991 analyzed by ChemCam at Pahrump Hills, Gale crater, Mars. *Icarus*, *281*, pp.121-136.
992 Nellessen, M.A., Baker, A.M., Newsom, H.E., Jackson, R.S., Nachon, M., Rivera-Hernandez,
993 F., Williams, J., Wiens, R.C., Frydenvang, J., Gasda, P., Lanza, N., Ollila, A., Clegg, S.,
994 Gasnault, O., Maurice, S., Meslin, P.Y., Cousin, A., Rapin, W., Lasue, J., Forni, O.,
995 L'Haridon, J, Blaney, D., Payré, V., Mangold, N., LeDeit, L., Edgett, K., Anderson, R.
996 Distribution and Analysis of Calcium Sulfate-Cemented Sandstones along the MSL
997 Traverse, Gale Crater, Mars. (March, 2018). In *Abstract 2858 presented at Lunar and*
998 *Planet. Sci. Conf* (Vol. 49).
999 Newsom, H., Edgett, K., Wiens, R., Mangold, N., Schieber, J., Stack, K., Rapin, W., Stein, N.,
1000 Rivera-Hernandez, F. (October, 2017). Imaging and chemical signatures of sandstone
1001 cemented by calcium sulfate, in the Stimson and Murray formation rocks of Gale Crater,
1002 Mars, International Meeting of Sedimentology 33, Toulouse, France.
1003 Palucis, M.C., Dietrich, W.E., Hayes, A.G., Williams, R.M., Gupta, S., Mangold, N., Newsom,
1004 H., Hardgrove, C., Calef, F. and Sumner, D.Y. (2014). The origin and evolution of the
1005 Peace Vallis fan system that drains to the Curiosity landing area, Gale Crater,
1006 Mars. *Journal of Geophysical Research: Planets*, *119*(4), pp.705-728.

1007 Rampe, E.B., Ming, D.W., Blake, D.F., Bristow, T.F., Chipera, S.J., Grotzinger, J.P., Morris,
1008 R.V., Morrison, S.M., Vaniman, D.T., Yen, A.S. and Achilles, C.N. (2017). Mineralogy
1009 of an ancient lacustrine mudstone succession from the Murray formation, Gale crater,
1010 Mars. *Earth and Planetary Science Letters*.
1011 Sautter, V., Fabre, C., Forni, O., Toplis, M.J., Cousin, A., Ollila, A.M., Meslin, P.Y., Maurice,
1012 S., Wiens, R.C., Baratoux, D. and Mangold, N. (2014). Igneous mineralogy at Bradbury
1013 Rise: The first ChemCam campaign at Gale crater. *Journal of Geophysical Research:*
1014 *Planets*, *119*(1), pp.30-46.
1015 Siebach, K.L., Grotzinger, J.P., Kah, L.C., Stack, K.M., Malin, M., Léveillé, R. and Sumner,
1016 D.Y. (2014). Subaqueous shrinkage cracks in the Sheepbed mudstone: Implications for
1017 early fluid diagenesis, Gale Crater, Mars. *Journal of Geophysical Research:*
1018 *Planets*, *119*(7), pp.1597-1613.
1019 Siebach, K.L., Baker, M.B., Grotzinger, J.P., McLennan, S.M., Gellert, R., Thompson, L.M.
1020 and Hurowitz, J.A. (2017). Sorting out compositional trends in sedimentary rocks of the
1021 Bradbury group (Aeolis Palus), Gale crater, Mars. *Journal of Geophysical Research:*
1022 *Planets*, *122*(2), pp.295-328.
1023 Sivakumar, P., Taleh, L., Markushin, Y., & Melikechi, N. (2014). Packing density effects on the
1024 fluctuations of the emission lines in laser-induced breakdown
1025 spectroscopy. *Spectrochimica Acta Part B: Atomic Spectroscopy*, *92*, 84-89.
1026 Stack, K.M., Grotzinger, J.P., Kah, L.C., Schmidt, M.E., Mangold, N., Edgett, K.S., Sumner,
1027 D.Y., Siebach, K.L., Nachon, M., Lee, R. and Blaney, D.L. (2014). Diagenetic origin of
1028 nodules in the Sheepbed member, Yellowknife Bay formation, Gale crater, Mars. *Journal*
1029 *of Geophysical Research: Planets*, *119*(7), pp.1637-1664.
1030 Stack, K.M., Grotzinger, J.P., Edgett, K.S., Gupta, S., Kah, L.C., Lamb, M.P, Lewis, K.W.,
1031 Rubin, D.M., Schieber, J., Sumner, D.Y. (2016, September) Facies analysis and
1032 stratigraphic context of the Pahrump Hills outcrop, type locality of the basal Murray formation,
1033 Gale Crater, Mars. Geological Society of America Abstract*,* Vol. 48, No. 7.
1034 Summons, R.E., Amend, J.P., Bish, D., Buick, R., Cody, G.D., Des Marais, D.J., Dromart, G.,
1035 Eigenbrode, J.L., Knoll, A.H. and Sumner, D.Y. (2011). Preservation of martian organic
1036 and environmental records: final report of the Mars Biosignature Working
1037 Group. *Astrobiology*, *11*(2), pp.157-181.
1038 Thomson, B.J., Bridges, N.T., Milliken, R., Baldridge, A., Hook, S.J., Crowley, J.K., Marion,
1039 G.M., de Souza Filho, C.R., Brown, A.J. and Weitz, C.M. (2011). Constraints on the
1040 origin and evolution of the layered mound in Gale Crater, Mars using Mars
1041 Reconnaissance Orbiter data. *Icarus*, *214*(2), pp.413-432.
1042 Vaniman, D., Dyar, M.D., Wiens, R., Ollila, A., Lanza, N., Lasue, J., Rhodes, J.M., Clegg, S.
1043 and Newsom, H. (2012). Ceramic ChemCam calibration targets on Mars science
1044 laboratory. *Space science reviews*, *170*(1-4), pp.229-255.
1045 Vaniman, D.T., Bish, D.L., Ming, D.W., Bristow, T.F., Morris, R.V., Blake, D.F., Chipera, S.J.,
1046 Morrison, S.M., Treiman, A.H., Rampe, E.B. and Rice, M. (2013). Mineralogy of a
1047 mudstone at Yellowknife Bay, Gale crater, Mars. *Science*, p.1243480.
1048 Vasavada, A.R., Grotzinger, J.P., Arvidson, R.E., Calef, F.J., Crisp, J.A., Gupta, S., Hurowitz,
1049 J., Mangold, N., Maurice, S., Schmidt, M.E. and Wiens, R.C. (2014). Overview of the
1050 Mars Science Laboratory mission: Bradbury landing to Yellowknife Bay and
1051 beyond. *Journal of Geophysical Research: Planets*, *119*(6), pp.1134-1161.
1052 Wentworth, C.K. (1922). A scale of grade and class terms for clastic sediments. *The Journal of*
1053 *Geology*, *30*(5), pp.377-392.

Wiens, R.C., Maurice, S., Barraclough, B., Saccoccio, M., Barkley, W.C., Bell, J.F., Bender, S., Bernardin, J., Blaney, D., Blank, J. and Bouyé, M., et al. (2012). The ChemCam instrument suite on the Mars Science Laboratory (MSL) rover: Body unit and combined system tests. *Space Science Reviews*, *170*(1-4), pp.167-227.

Wiens, R. C., Maurice, S., Lasue, J., Forni, O., Anderson, R. B., Clegg, S., et al. (2013). Pre-flight calibration and initial data processing for the ChemCam laser-induced breakdown spectroscopy instrument on the Mars Science Laboratory rover. Spectrochimica Acta Part B: Atomic Spectroscopy, 82, 1-27.

Wiens R.C., Maurice S., and Rull Perez F. (2017) The SuperCam remote sensing instrument suite for the Mars 2020 rover mission: A preview. Spectroscopy 32(5), 50-55.

Williams, R.M., Grotzinger, J.P., Dietrich, W.E., Gupta, S., Sumner, D.Y., Wiens, R.C., Mangold, N., Malin, M.C., Edgett, K.S., Maurice, S. and Forni, O. (2013). Martian fluvial conglomerates at Gale crater. *science*, *340*(6136), pp.1068-1072.

Yingst, R. A., Edgett, K. S., Kennedy, M. R., Krezoski, G. M., McBride, M. J., Minitti, M. E., Ravine, M. A., and Williams, R. M. E. (2016). MAHLI on Mars: lessons learned operating a geoscience camera on a landed payload robotic arm. *Geoscientific Instrumentation, Methods and Data Systems*, *5*, 205-217.

11. Figure Captions

Figure 1. a) A mosaic of Gale Crater using images taken by the Mars Reconnaissance Orbiter Context Camera. A list of the images used in this mosaic is provided by Anderson and Bell (2010). The black box highlights the area shown in Figure 1b. b) A mosaic of the *Curiosity* field area using images taken by the High Resolution Imaging Science Experiment camera on the Mars Reconnaissance Orbiter. The white line shows the rover traverse path between landing and sol 1850. The yellow star marks the landing site of *Curiosity*, the orange star marks the location of Yellowknife Bay, and the red star that of Pahrump Hills. The green highlighted area is the mapped aerial extent of the Murray formation from Fraeman et al. (2016).

Figure 2. Schematic showing the relationship between the LIBS laser spot diameter and grain size. Rocks with grains smaller than the laser spot size yield the bulk rock compositions at each LIBS spot, whereas those with grains about the size or larger can have chemical contributions from individual grains at each spot, producing non-uniform compositions.

Figure 3. G_{MEAN} for the rocks used in the GIMS analysis plotted with the stratigraphic column of the Yellowknife Bay formation constructed using outcrop elevation (Grotzinger et al., 2014). The four GSRs were defined during the calibration procedure (see Section 5.2). GSR3 has a hashed pattern because its bounds are not well constrained.

Figure 4. G_{MEAN} for the rocks from Pahrump Hills used in the GIMS analysis plotted with the stratigraphic column of the Pahrump Hills member of the Murray formation constructed using outcrop elevation (Stack et al., 2016). The four GSRs were defined during the calibration procedure (see Section 5.2). GSR3 has a hashed pattern because its bounds are not well constrained.

Figure 5. Cropped RMI image mosaics of the ChemCam targets Nanok (a), Gillespie_Lake_1 (b), and Wakham_Bay (c). The red crosshairs mark the locations of LIBS laser spots on the rock targets. The low depth of field of RMI images results in some parts of the mosaics being out of focus. For Wakham_Bay (c), the laser hit a very coarse sand sized grain at point 12 and a granule at point 15.

Figure 6. a) Cropped RMI image of the Aztec_2 ChemCam target. Orange arrows highlight sand sized voids. b) Oblique MAHLI image of the upper Chinle outcrop, showing low angle cross-stratification, marked by the white arrows. MAHLI product 0828MH0004520020301655C00. c) Cropped MAHLI image of the Whale Rock outcrop. Sand grains can clearly be resolved in the image. MAHLI product 0860MH0004580000302120R00. d) Mastcam (M-100) mosaic of the Whale Rock outcrop. White arrows highlight climbing-ripple cross-stratification. Mastcam products 0796MR0034760210500167E01 and 0796MR0034760220500168E01.

Figure 7. a) Cropped Mastcam (M-34) of the rock with the Gillespie_Lake_1 and Gillespie_Lake_2 analyses. Mastcam product 0132ML0008020000103972E01. b) Cropped Mastcam (M-100) of the rock with the Rocknest_3, Rocknest_3a, and Rocknest_3b analyses. Mastcam product 0086MR0003750000104151E0. For both (a) and (b) the approximate locations of the LIBS analyses are highlighted by white rectangles.

Figure 8. Grain size from image-data versus G_{MEAN} for the rocks of the Yellowknife Bay formation and Pahrump Hills member. The four GSRs were defined during the calibration procedure (see Section 5.2). GSR3 has a hashed pattern because its bounds are not well constrained. Each data point includes 1σ STDr horizontal error bars and a grey vertical box showing the range of observed grain sizes in image data. Most samples may include finer grain sizes that could not be resolved in the images.

12. Supplemental tables

Supplemental Table 1. The ChemCam LIBS data used in the GIMS analysis. Only data that passed through the filtering procedure described in Section 2.2 are included. The accuracy (oxide RMSEP) and precision (oxide_shots_stdev) are included for every major-element oxide per LIBS point.

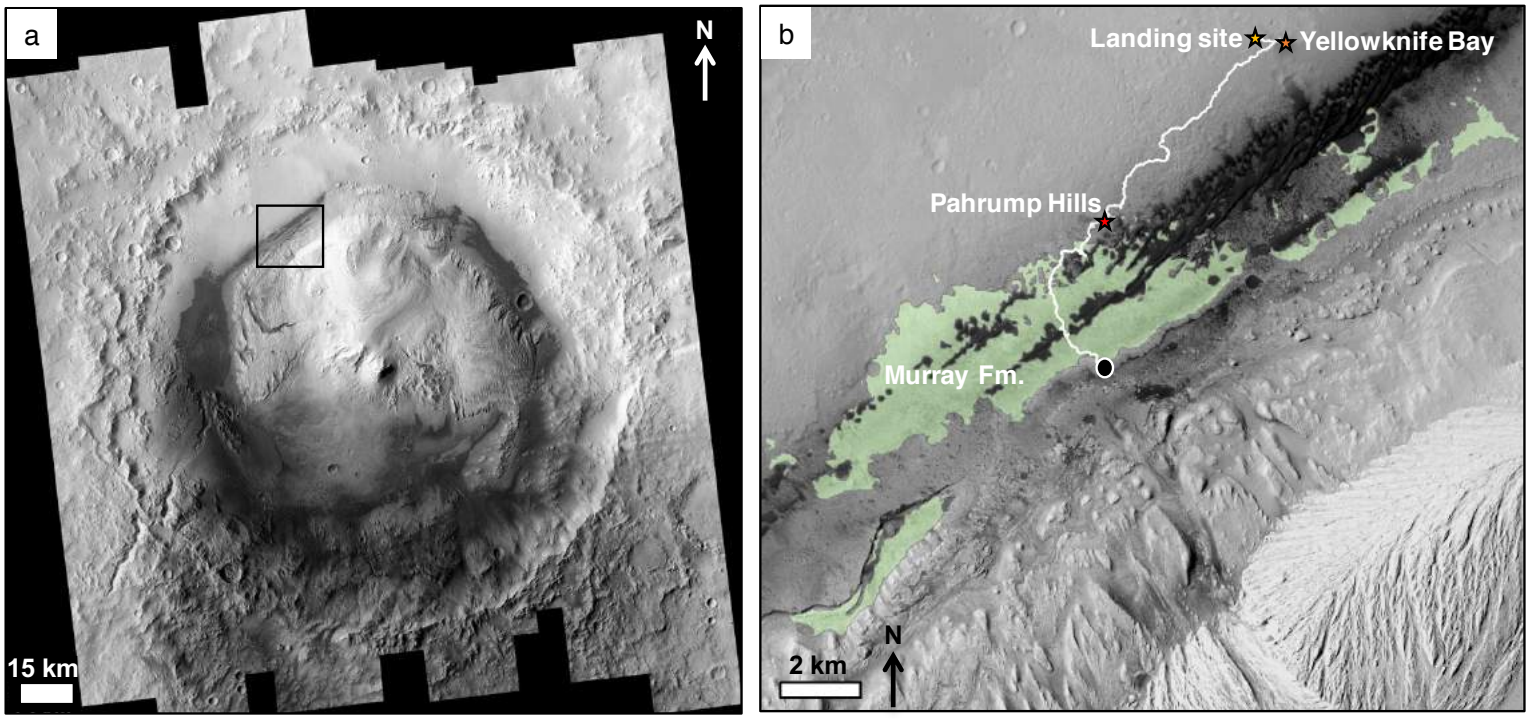
a
N
15 km
b
Landing site
Yellowknife Bay
Pahrump Hills
Murray Fm.
2 km
N

Figure 1.

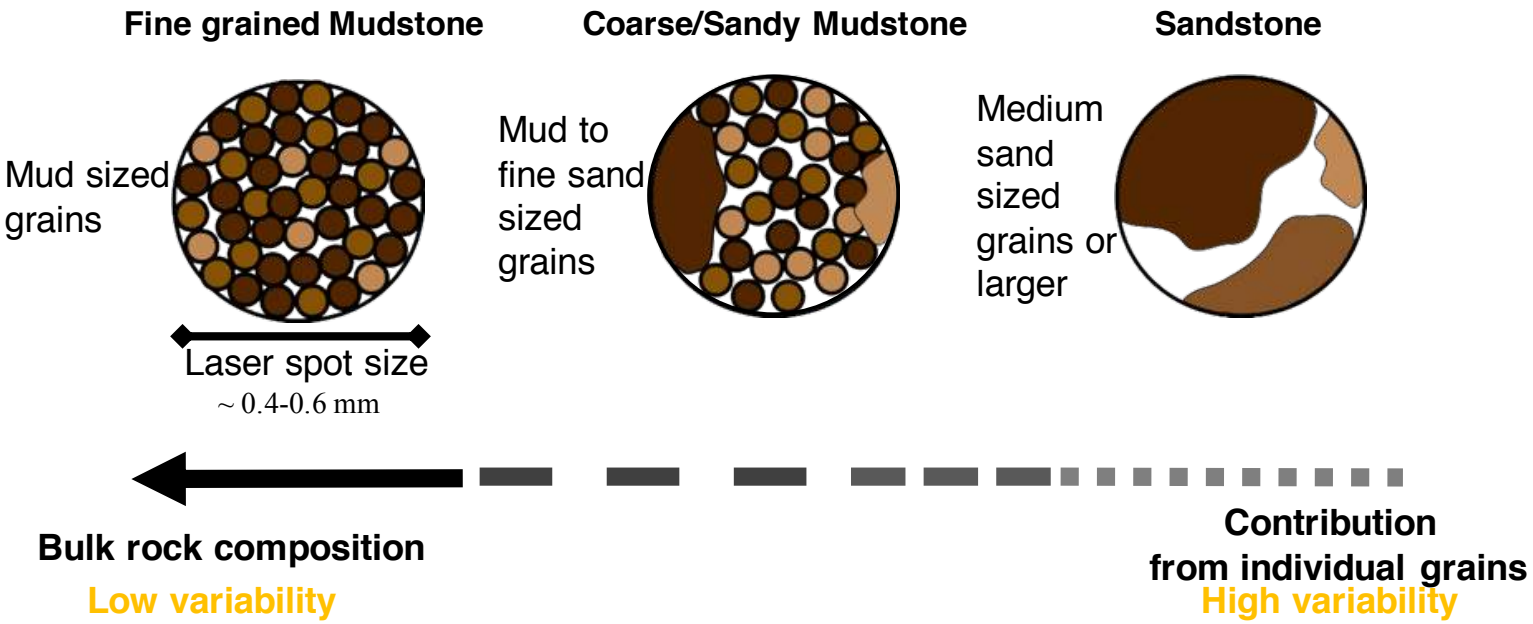
Fine grained Mudstone
Coarse/Sandy Mudstone
Sandstone
Mud sized grains
Mud to fine sand sized grains
Medium sand sized grains or larger
Laser spot size
~ 0.4-0.6 mm
Bulk rock composition
Low variability
Contribution from individual grains
High variability

Figure 2.

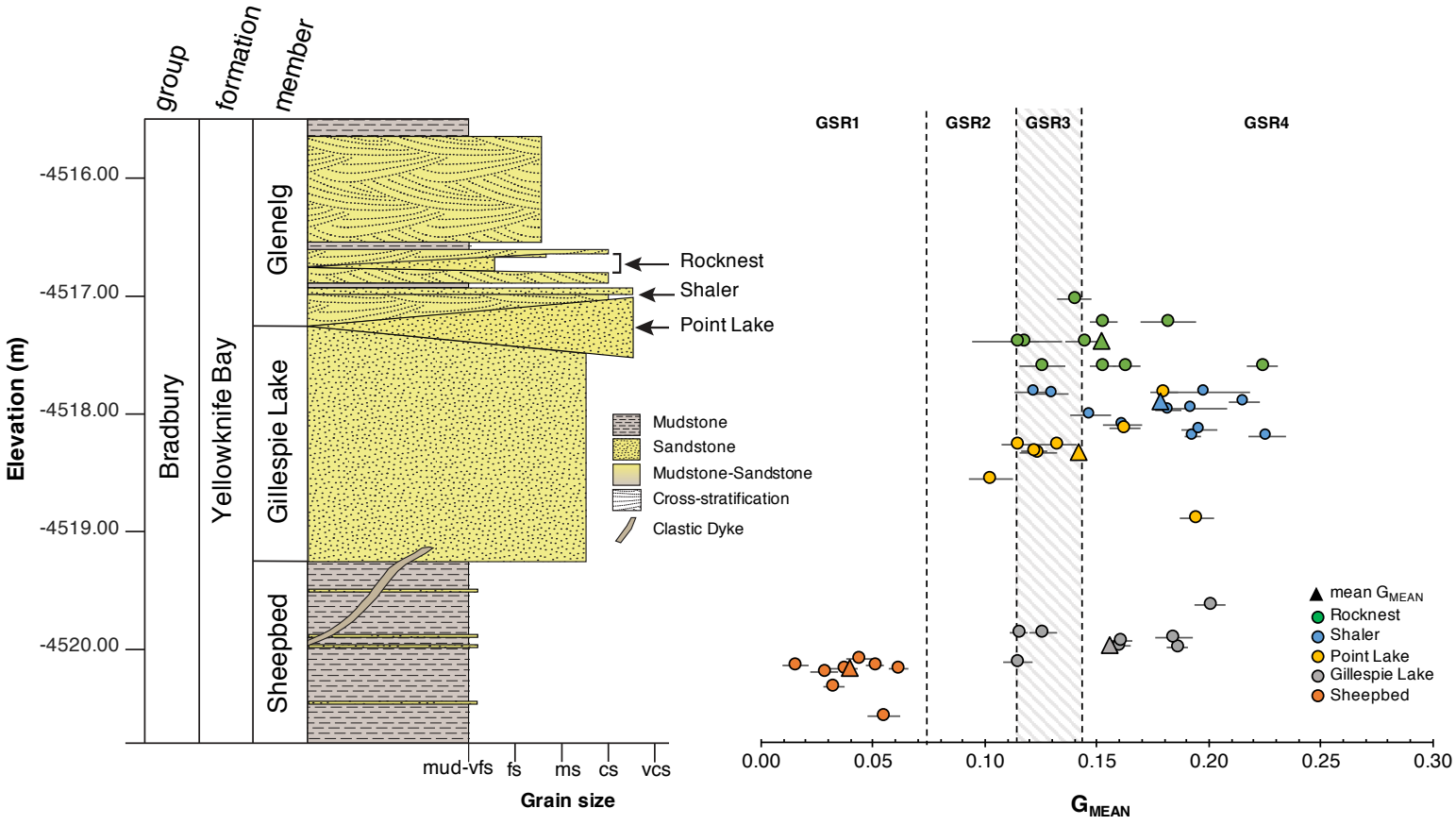
group
formation
member
Bradbury
Yellowknife Bay
Glenelg
Gillespie Lake
Sheepbed
Elevation (m)
-4516.00
-4517.00
-4518.00
-4519.00
-4520.00
Rocknest
Shaler
Point Lake
Mudstone
Sandstone
Mudstone-Sandstone
Cross-stratification
Clastic Dyke
mud-vfs
fs
ms
cs
vcs
Grain size
GSR1
GSR2
GSR3
GSR4
0.00
0.05
0.10
0.15
0.20
0.25
0.30
G_MEAN
mean G_MEAN
Rocknest
Shaler
Point Lake
Gillespie Lake
Sheepbed

Figure 3.

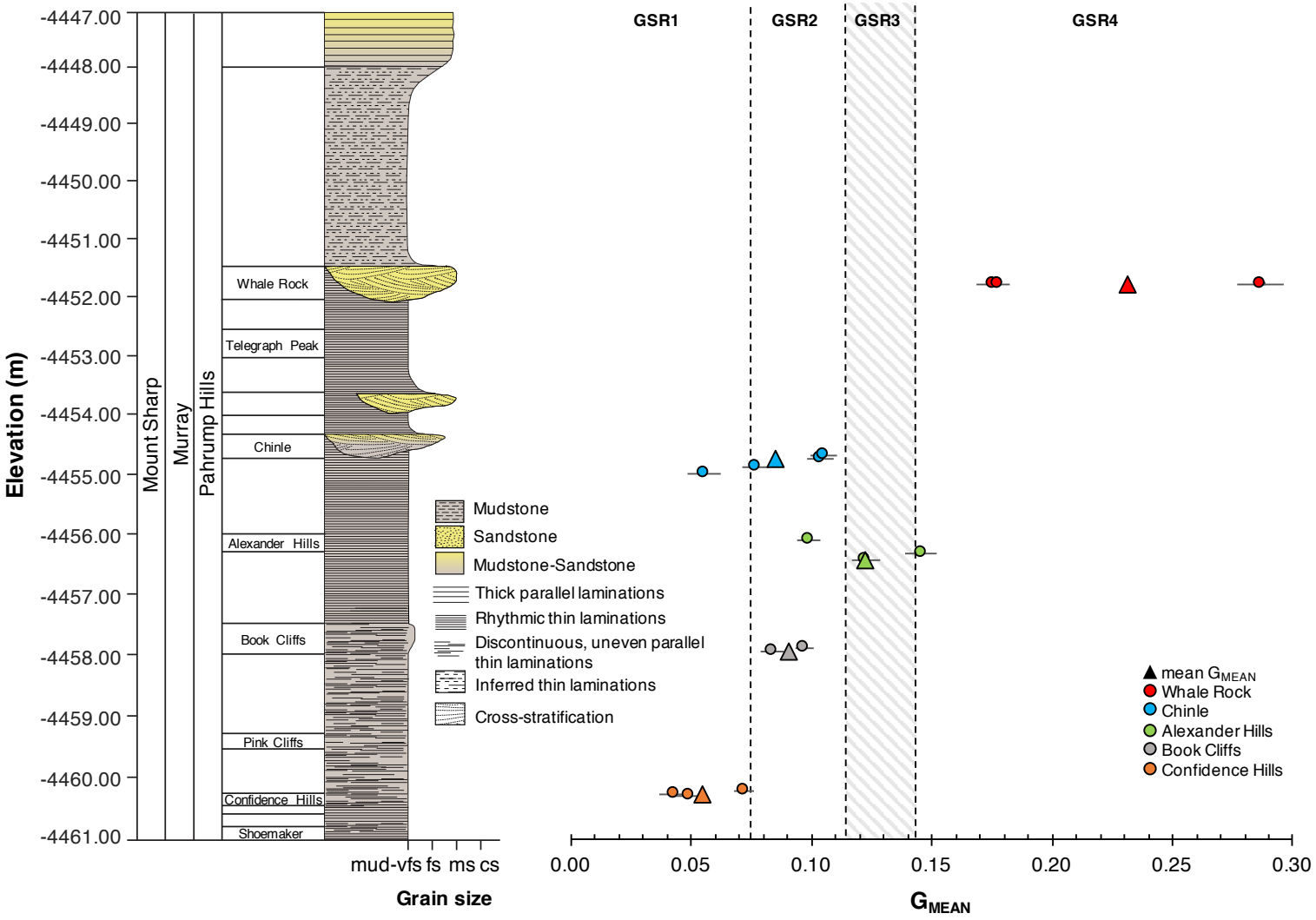
Elevation (m)
-4447.00
-4448.00
-4449.00
-4450.00
-4451.00
-4452.00
-4453.00
-4454.00
-4455.00
-4456.00
-4457.00
-4458.00
-4459.00
-4460.00
-4461.00
Mount Sharp
Murray
Pahrump Hills
Whale Rock
Telegraph Peak
Chinle
Alexander Hills
Book Cliffs
Pink Cliffs
Confidence Hills
Shoemaker
mud-vfs fs ms cs
Grain size
Mudstone
Sandstone
Mudstone-Sandstone
Thick parallel laminations
Rhythmic thin laminations
Discontinuous, uneven parallel thin laminations
Inferred thin laminations
Cross-stratification
GSR1
GSR2
GSR3
GSR4
mean G_MEAN
Whale Rock
Chinle
Alexander Hills
Book Cliffs
Confidence Hills
0.00
0.05
0.10
0.15
0.20
0.25
0.30
G_MEAN

Figure 4.

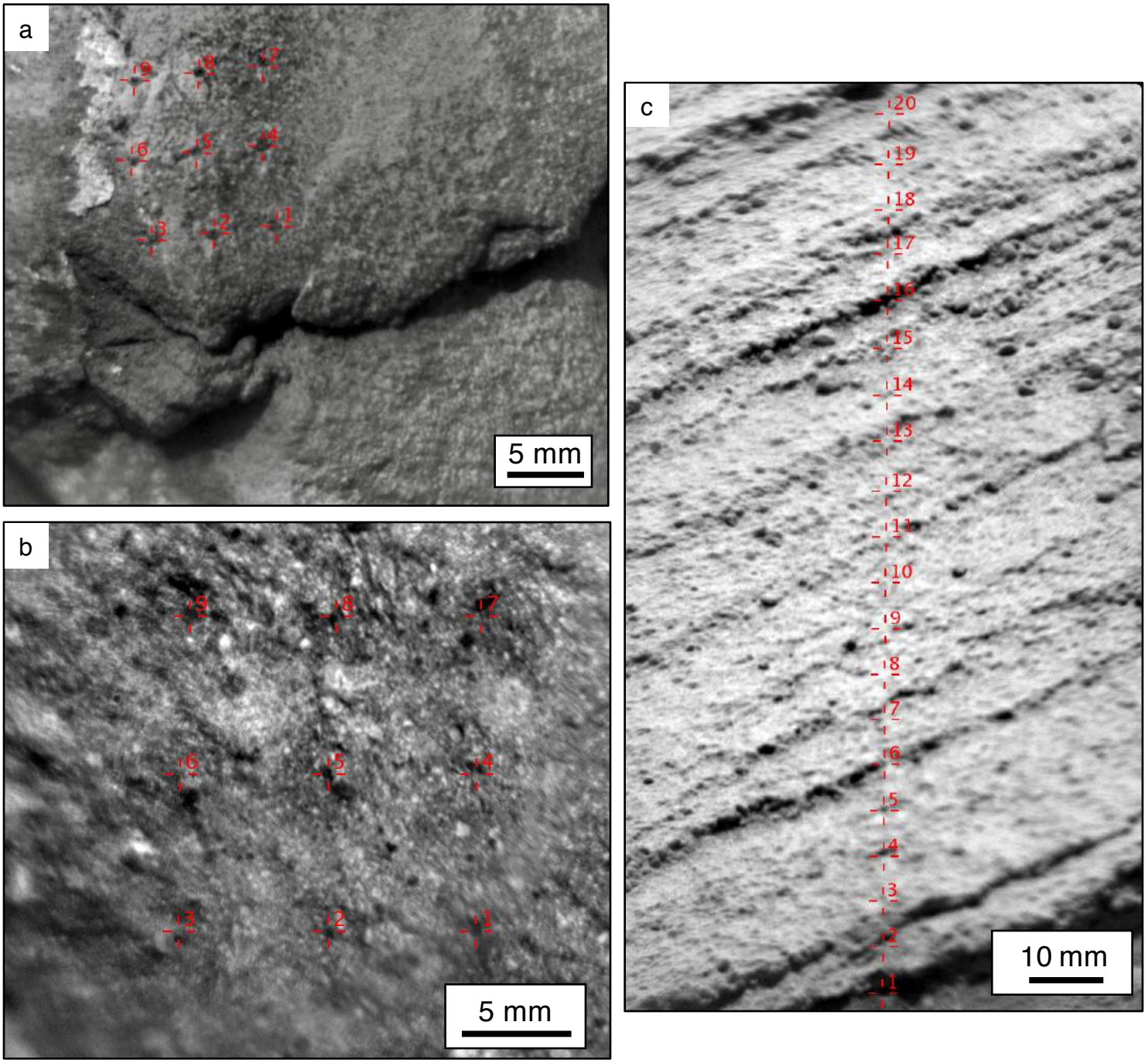
a
9
8
7
6
5
4
3
2
1
5 mm
b
9
8
7
6
5
4
3
2
1
5 mm
c
20
19
18
17
16
15
14
13
12
11
10
9
8
7
6
5
4
3
2
1
10 mm

Figure 5.

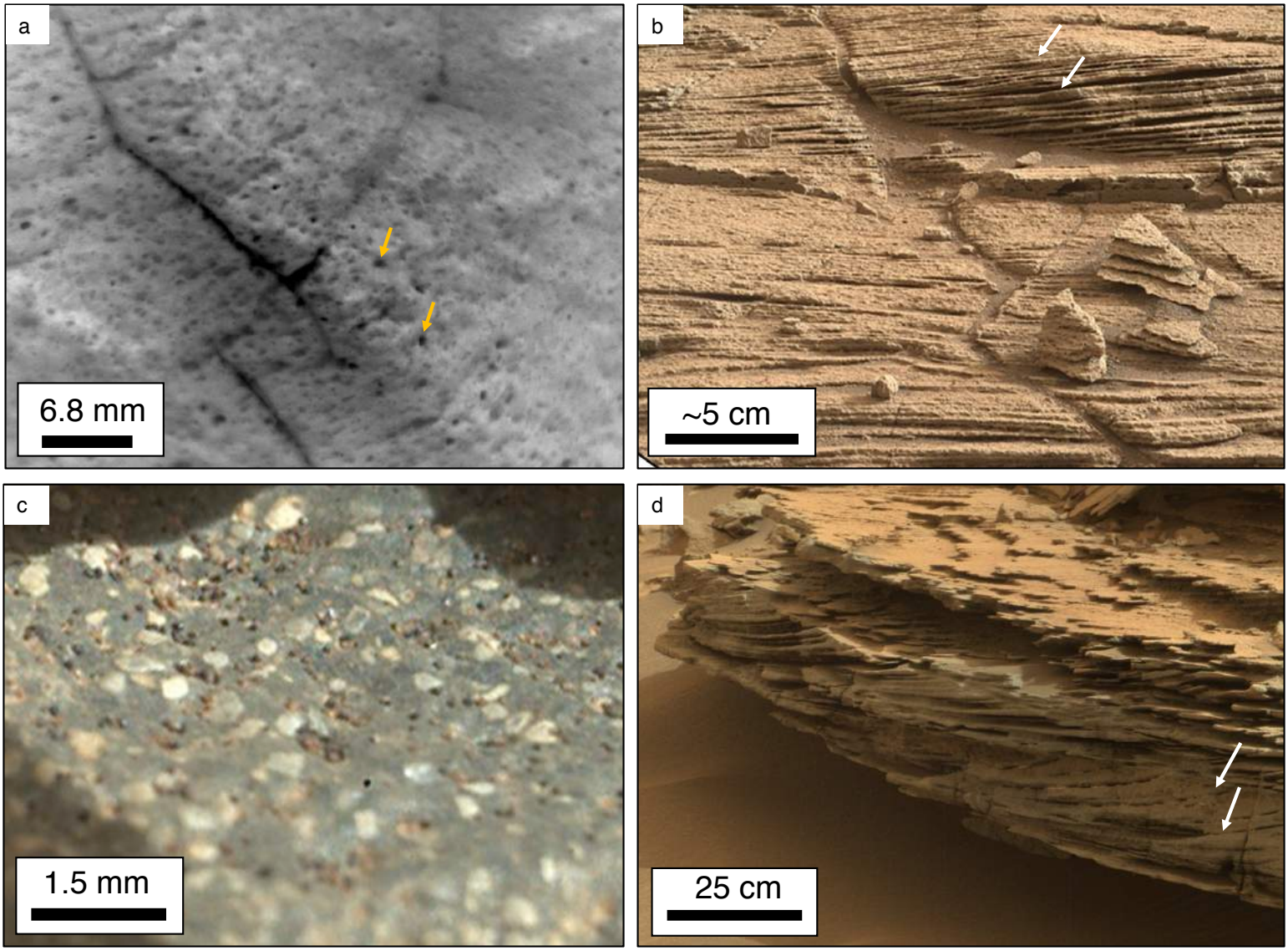

Figure 6.

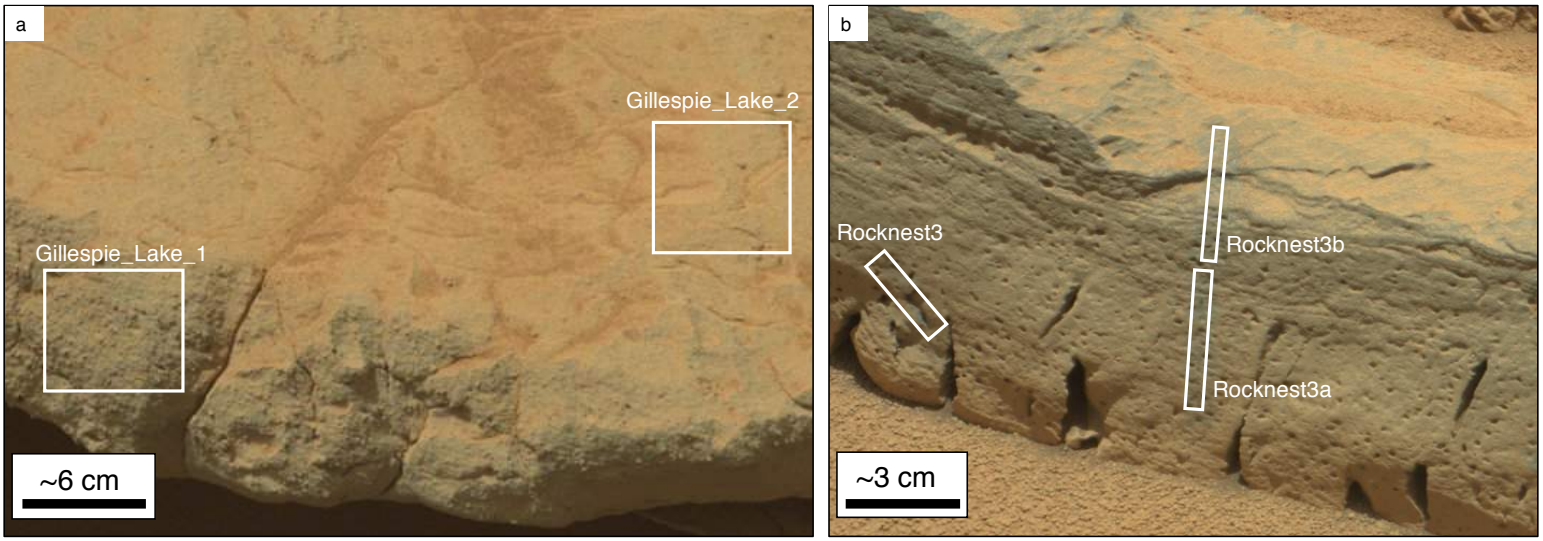
a
Gillespie_Lake_2
Gillespie_Lake_1
~6 cm
b
Rocknest3
Rocknest3b
Rocknest3a
~3 cm

Figure 7.

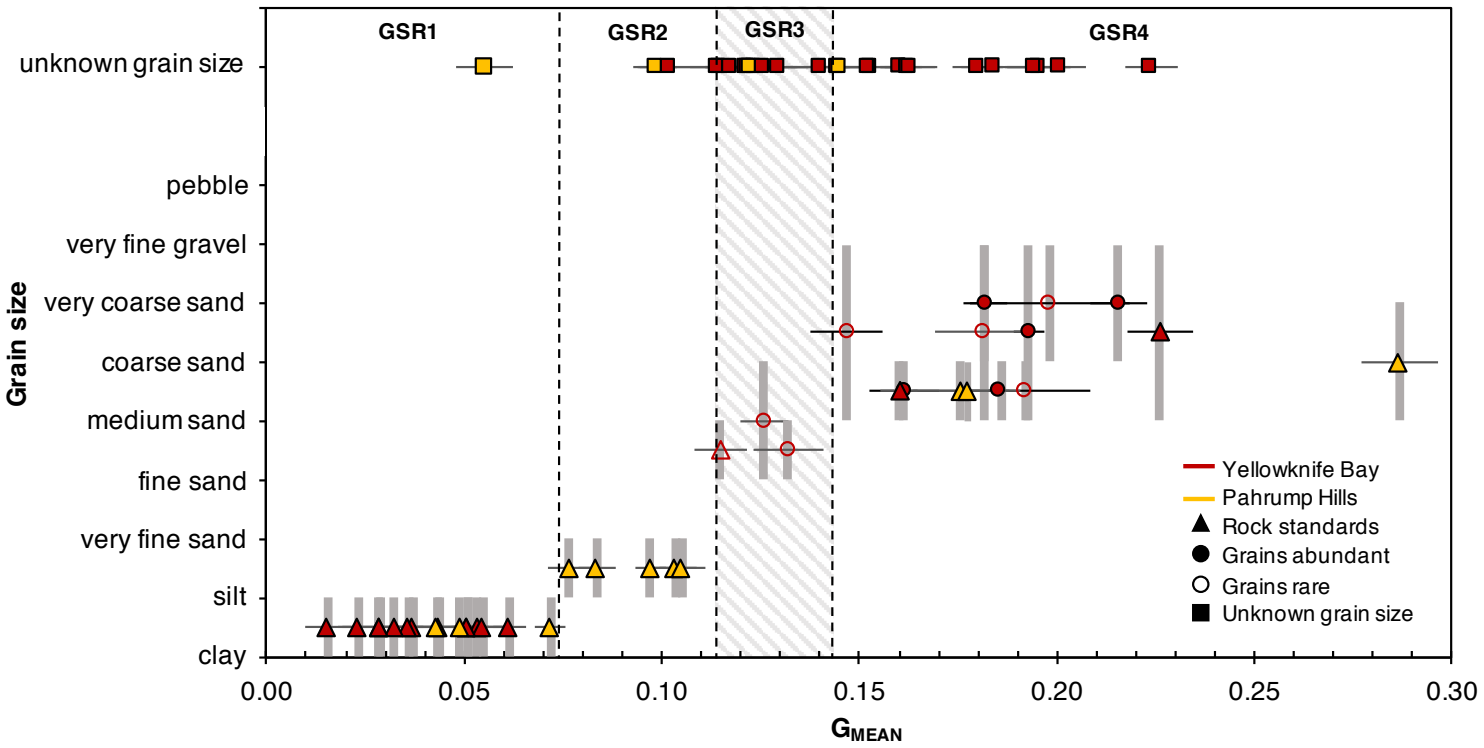
GSR1
GSR2
GSR3
GSR4
unknown grain size
pebble
very fine gravel
very coarse sand
coarse sand
medium sand
fine sand
very fine sand
silt
clay
Grain size
0.00
0.05
0.10
0.15
0.20
0.25
0.30
G_MEAN
Yellowknife Bay
Pahrump Hills
Rock standards
Grains abundant
Grains rare
Unknown grain size

Figure 8.

11. Tables

Table 1. Rocks that were used as calibration standards for the GIMS reported in each grain size range considered. The GSRs were defined based on G_{MEAN} values. Grain size estimates for the rock standards at Yellowknife Bay were based on previous studies or made directly using RMI images, whereas for the rock standards at Pahrump Hills, grain size estimates were made by using MAHLI images of nearby regions or directly using RMI images. RMI image grain size estimates are for grains near the laser pits. Numerical values for grain size are reported for the bulk of the grains.

Target Names	Locality and Member/Outcrop	Image-based grain size estimate and instrument used for measurements	Sorting Estimate	Min and max G_{MEAN}	Grain Size Regime
Sheepbed Beachrock Belcher Flaherty Richardson Flaherty_2 Barn_2 Rackla Haig Hudson_Bay Nastapoka Wernecke_1 Rae2	Sheepbed, YKB	Mud, <62.5 μm (Grotzinger et al., 2014; 2015)	Well sorted	0.01, 0.06	GSR1
The_Maze Crowley Hanaupah	Confidence Hills, PH	Mud to silty/sandy mud, <125 μm (MAHLI)	Moderately well sorted	0.04, 0.07	GSR1
Goblin_Valley, Deadman_Pass, Sespe, Aguereberry_Point, Soledad_Pass	Book Cliffs, and Chinle, PH	Silt to very fine sand, 62.5-125.0 μm (MAHLI)	Moderately well sorted	0.08, 0.11	GSR2
Nanok	Gillespie Lake Member, YKB	Fine to medium sand sized grains with sparse coarse sand, 0.125-0.500 mm (RMI)	Moderately well sorted	0.11	GSR3
Gillespie_Lake_1	Gillespie Lake Member, YKB	Medium sand to coarse sand with sparse very coarse sand, 0.5-1.0 mm (RMI)	Poorly sorted	0.16	GSR4
Wakham_Bay	Glenelg Member, Shaler, YKB	Medium to very coarse sand size sediment with sparse granules, 0.5-2.0 mm (RMI)	Moderately to poorly sorted	0.23	GRS4
Orocopia Vasquez, Wild_Horse_Mesa_	Whale Rock, PH	Medium to coarse sand with sparse very coarse sand in a matrix of finer sediment, 0.5-1.0 mm (MAHLI & RMI)	Poorly to very poorly sorted	0.18, 0.29	GSR4

Table 2. All targets used in the GIMS analysis, with summary information, including independent grain size estimates if known and G_{MEAN}. Two standard deviation metrics are reported for each G_{MEAN}, STDr and STDc, derived from standard deviations for each LIBS point and oxide on rock (STDr) or the Shergottite calibration target (STDc). Grain size estimates for rocks at Yellowknife Bay are for grains near the laser pits in RMI images. For rocks at Pahrump Hills, grain size estimates were indirectly made by using MAHLI images of regions near the ChemCam analyses. Rocks with G_{MEAN}=0.11 are reported as GSR2/GSR3. Target names are merged in the same cell for those analyses that were taken on the same rock exposure and those with asterisks are calibration standards.

Formation /Outcrop	Member /Unit	Target Name	Sequence ID	Sol	Elevation (m)	# of points used	Raster type	G_{MEAN}	STDr (1σ)	STDc (1σ)	mean G_{MEAN}	Grain size estimate	GSR
Pahrump Hills	Confidence Hills	The_Maze*	ccam02767	766	-4460.28	8	3x3	0.05	0.01	0.00	0.05	Mud with silt to very fine sand	GSR1
		Crowley*	ccam04771	770	-4460.26	9	1x10	0.04	0.01	0.00		Mud with silt to very fine sand	GSR1
		Hanaupah*	ccam03779	778	-4460.21	9	3x3	0.07	0.00	0.00		Mud with silt to very fine sand	GSR1
	Book Cliffs	Goblin_Valley*	ccam01787	786	-4457.83	10	1x10	0.10	0.00	0.00	0.09	Silt to very fine sand	GSR2
		Deadman_Pass*	ccam02787	786	-4457.88	8	1x10	0.08	0.00	0.00		Silt to very fine sand	GSR2
	Alexander Hills	Cajon	ccam01792	791	-4456.01	10	1x10	0.10	0.00	0.00	0.12	Voids and dark features that are silt/very fine sand to very coarse sand in size	GSR2
		Agate_Hill	ccam02792	791	-4456.36	10	1x10	0.12	0.01	0.00		Voids and dark features that are silt/very fine sand to very coarse sand in size	GSR3

		Aztec_2	ccam03792	791	-4456.24	10	1x10	0.15	0.01	0.00		Voids and dark features that are silt/very fine sand to very coarse sand in size	GSR4
	Chinle	Cima	ccam01794	793	-4454.92	5	1x10	0.06	0.01	0.00	0.09	Uncertain from RMI mosaic and no MAHLI taken nearby	GSR1
		Sespe*	ccam02794	793	-4454.78	10	1x10	0.08	0.01	0.00		Silt to very fine sand	GSR2
		Aguereberry Point*	ccam03794	793	-4454.65	5	1x10	0.10	0.01	0.00		Silt to very fine sand	GSR2
		Soledad_Pass*	ccam04794	793	-4454.60	9	1x10	0.11	0.01	0.01		Silt to very fine sand	GSR2/ GSR3
	Whale Rock	Orocopia*	ccam01796	795	-4451.73	9	1x10	0.29	0.01	0.00	0.21	Medium to very coarse sand	GSR4
		Wild_Horse_ Mesa*	ccam03796	795	-4451.73	8	1x10	0.18	0.01	0.00		Medium to coarse sand in a finer grained matrix	GSR4
		Vasquez*	ccam04796	795	-4451.73	8	1x10	0.18	0.01	0.01		Medium to coarse sand in a finer grained matrix	GSR4
		Sheepbed*	ccam01126	125	-4520.33	9	3x3	0.06	0.00	0.00	0.04	Mud (Grotzinger et al., 2014; 2015)	GSR1
		Beachrock*	ccam02126	125	-4520.33	9	3x3	0.04	0.01	0.00		Mud (Grotzinger et al., 2014; 2015)	GSR1

Yellowknife Bay	Sheepbed	Belcher*	ccam01127	126	-4521.07	9	3x3	0.02	0.00	0.00		Mud (Grotzinger et al., 2014; 2015)	GSR1
		Flaherty*	ccam01129	128	-4521.33	5	1x5	0.05	0.01	0.00		Mud (Grotzinger et al., 2014; 2015)	GSR1
		Richardson*	ccam02129	128	-4521.31	5	5x1	0.03	0.01	0.00		Mud (Grotzinger et al., 2014; 2015)	GSR1
		Flaherty_2*	ccam01130	129	-4521.32	5	1x5	0.04	0.01	0.00		Mud (Grotzinger et al., 2014; 2015)	GSR1
		Barn_2*	ccam03130	129	-4521.06	5	5x1	0.05	0.01	0.00		Mud (Grotzinger et al., 2014; 2015)	GSR1
		Rackla*	ccam05135	134	-4520.76	8	3x3	0.05	0.01	0.00		Mud (Grotzinger et al., 2014; 2015)	GSR1
		Haig*	ccam01150	150	-4520.30	5	5x1	0.02	0.01	0.00		Mud (Grotzinger et al., 2014; 2015)	GSR1
		Hudson_Bay*	ccam04150	150	-4520.50	8	3x3	0.03	0.00	0.00		Mud (Grotzinger et al., 2014; 2015)	GSR1
		Nastapoka*	ccam03160	159	-4520.25	9	3x3	0.04	0.01	0.00		Mud (Grotzinger et al., 2014; 2015)	GSR1
		Wernecke_1*	ccam01172	171	-4520.36	9	3x3	0.03	0.01	0.00		Mud (Grotzinger et al., 2014; 2015)	GSR1
		Rae2*	ccam02192	191	-4520.31	9	3x3	0.05	0.00	0.00		Mud (Grotzinger et al., 2014; 2015)	GSR1

	Gillespie Lake	Gillespie_Lake_1* Gillespie_Lake_2	ccam01132	132	-4520.13	8	3x3	0.16	0.00	0.00		Medium to coarse sand size grains with sparse very coarse sand	GSR4
			ccam02132	132	-4520.09	8	3x3	0.16	0.01	0.00		Too dusty	GSR4
		Laddie	ccam01151	150	-4520.14	7	3x3	0.19	0.00	0.00		Medium to coarse sand sized grains	GSR4
		Kipalu	ccam03157	156	-4519.76	9	3x3	0.20	0.01	0.00		Too dusty	GSR4
		Nanok*	ccam02176	175	-4520.28	9	3x3	0.11	0.01	0.00	0.16	Fine to medium sand with sparse coarse sand. Fine sand is at resolution of RMI mosaic.	GSR2/ GSR3
		Jolliffe	ccam01181	180	-4520.01	10	10x1	0.12	0.00	0.00		RMI out of focus near raster	GSR3
		Doublet	ccam01186	185	-4520.00	10	1x10	0.13	0.01	0.00		Fine to coarse sand. Fine sand is at resolution of RMI mosaic.	GSR3
		Mugford	ccam02186	185	-4520.05	5	1x10	0.18	0.01	0.00		Uncertain	GSR4
	Glenelg, Point Lake	Acasta	ccam01104	103	-4518.38	7	3x3	0.12	0.01	0.00	0.14	Too dusty	GSR3
		Amagok	ccam01111	110	-4518.16	8	3x3	0.16	0.01	0.00		RMI mosaic out of focus	GSR4
		Ingraham	ccam01116	115	-4517.84	8	3x3	0.18	0.01	0.00		Too dusty	GSR4
		Kapvik	ccam02123	122	-4518.36	9	3x3	0.12	0.01	0.00		Too dusty	GSR3

	outcrop	Athole_Point	ccam02302	301	-4518.97	7	3x3	0.19	0.01	0.00		Uncertain	GSR4
		Balboa_ Dismal_Lakes Balboa_2	ccam01303	302	-4518.31	9	3x3	0.13	0.01	0.00		RMI mosaic has faded color. Could identify fine to medium sand with sparse coarse sand.	GSR3
			ccam02305	305	-4518.31	9	3x3	0.11	0.01	0.00		Uncertain	GSR2/ GSR3
		LeRoux	ccam01304	303	-4518.62	6	3x3	0.10	0.01	0.00		RMI mosaic out of focus	GSR2
	Glenelg, Shaler outcrop	Rove	ccam01309	308	-4517.93	14	20x1	0.22	0.01	0.00	0.18	Coarse sand to very fine gravel. Point 1 hit a granule.	GSR4
		Ramah	ccam02309	308	-4517.85	5	5x1	0.13	0.01	0.00		Too dusty	GSR3
		Michigamme	ccam01311	310	-4518.23	19	1x20	0.19	0.00	0.00		Medium sand to very fine gravel. Points 6,14, and 15 hit very coarse sand grains.	GSR4
		Saglek	ccam03315	314	-4518.17	7	3x3	0.20	0.01	0.00		Too dusty	GSR4
		Rusty_Shale	ccam01316	315	-4518.00	10	10x1	0.18	0.01	0.00		Coarse sand to very fine gravel.	GSR4

												Point 1 hit a granule.	
		Montaigne	ccam01317	316	-4518.13	11	4x4	0.16	0.01	0.00		Medium to coarse sand with sparse very coarse sand.	GSR4
		Aillik	ccam01319	318	-4517.98	7	3x3	0.19	0.02	0.01		Medium to coarse sand	GSR4
		Wakham_Bay*	ccam04311	310	-4518.23	19	1x20	0.23	0.01	0.00		Medium to very fine gravel. Point1 12 hit very coarse sand sized grain and point 15 hit a granule.	GSR4
		Chioak	ccam01315	314	-4518.05	9	3x3	0.15	0.01	0.00		Medium sand to very fine gravel	GSR4
		Mary_River	ccam04316	315	-4517.84	9	3x3	0.20	0.02	0.01		Coarse sand to very fine gravel	GSR4
		Menihek	ccam03319	318	-4517.84	9	3x3	0.12	0.01	0.00		Uncertain	GSR3
	Glenelg, Rocknest outcrop	Rocknest3	ccam01057	56	-4517.60	5	1x5	0.13	0.01	0.00	0.15	Uncertain	GSR3
		Rocknest3a	ccam01082	81	-4517.60	10	1x10	0.15	0.01	0.00		Uncertain	GSR4
		Rocknest3b	ccam01083	83	-4517.60	10	1x10	0.16	0.00	0.00		Uncertain	GSR4
		Pearson_1	ccam02067	67	-4517.00	5	3x3	0.18	0.01	0.00		Medium to very fine gravel	GSR4
		Pearson_2	ccam02079	78	-4517.21	8	3x3	0.15	0.01	0.00		Too dusty	GSR4
		Rocknest6	ccam01071	70	-4517.50	5	3x3	0.12	0.01	0.00		Uncertain	GSR3

		Rocknest6a Rocknest6b	ccam04087	87	-4517.50	9	3x3	0.14	0.01	0.00		Uncertain	GSR3
			ccam05087	87	-4517.50	5	3x3	0.11	0.02	0.01		Uncertain	GSR2/ GSR3
		Peg	ccam03071	70	-4517.00	9	3x3	0.14	0.01	0.00		Uncertain	GSR3